

On the transient response of serpentine (antigorite) gouge to stepwise changes in slip velocity under high-temperature conditions

Miki Takahashi,¹ Shin-Ichi Uehara,^{1,2} Kazuo Mizoguchi,³ Ichiko Shimizu,⁴ Keishi Okazaki,⁵ and Koji Masuda¹

Received 25 October 2010; revised 31 May 2011; accepted 20 July 2011; published 18 October 2011.

[1] Shear-sliding tests were conducted on serpentine (antigorite) gouge to understand the rheology of serpentine-bearing faults. The experiments were carried out using a constant confining pressure (100 MPa), a constant pore water pressure (30 MPa), and a range of temperatures (from room temperature to 600°C). The transient response in frictional behavior following stepwise changes in the slip velocity were documented at each temperature. Slip rates varied between 0.0115 and 11.5 $\mu\text{m/s}$. Both the general level of frictional strength and the transient responses changed drastically at around 450°C. As the temperature increased from 400°C to 450°C, the strength of antigorite rose sharply. The transient response also indicated a change in the mode of deformation from flow-type behavior at temperatures below 400°C to frictional behavior (stick-slip) at temperatures above 450°C–500°C. Although only a limited volume of serpentine was involved in the dehydration reaction, X-ray diffraction analyses and scanning electron microscopy observations showed that forsterite had nucleated in the experimental products at the higher temperatures that were associated with frictional behavior. Submicron-sized, streaky forsterite masses in shear-localized zones may be evidence of shear-induced dehydration that caused strengthening and embrittlement of the gouge. Although antigorite rheology is complicated, the subsequent change in friction coefficient per order-of-magnitude change in sliding velocity increased with both increasing temperature and decreasing velocity, implying that a possible flow mechanism of intragranular deformation became activated.

Citation: Takahashi, M., S.-I. Uehara, K. Mizoguchi, I. Shimizu, K. Okazaki, and K. Masuda (2011), On the transient response of serpentine (antigorite) gouge to stepwise changes in slip velocity under high-temperature conditions, *J. Geophys. Res.*, 116, B10405, doi:10.1029/2010JB008062.

1. Introduction

[2] The complicated rheology of serpentine is not fully understood, which is one of the motivations for this experimental study of its behavior during deformation. Sliding deformation tests were conducted on a simulated serpentine (antigorite) gouge at temperatures from room temperature to high temperature; dehydration was induced under constant confining (100 MPa) and pore water pressure (30 MPa)

conditions. At each temperature, stepwise changes in the slip velocity were imposed and the resulting, transient responses in friction were documented.

[3] Serpentine is common in oceanic rocks at transform faults, subduction boundaries [e.g., Christensen, 1972; Iwamori, 1998], and mantle wedges [e.g., Hacker *et al.*, 2003a, 2003b; Hilairet *et al.*, 2007; Hilairet and Reynard, 2009], and the seismic behavior and physical properties of serpentine-bearing faults have been widely debated. Long-standing issues are whether serpentinite is the cause for the creeping and weakness of the San Andreas fault [e.g., Moore and Rymer, 2007; Moore and Lockner, 2008] and whether dehydration of serpentinite is a cause for intermediate-depth earthquakes in subducting slabs [e.g., Peacock, 2001; Seno *et al.*, 2001; Hacker *et al.*, 2003a, 2003b; Jung *et al.*, 2009; Chernak and Hirth, 2010].

[4] Numerous experimental studies have investigated the structural competence of serpentine [e.g., Shimamoto, 1985; Moore *et al.*, 1986, 1996, 1997; Reinen *et al.*, 1991, 1994]. Some researchers have suggested that because serpentine is weaker than other minerals and rocks, it stabilizes faults by

¹Geological Survey of Japan, National Institute of Advanced Industrial Science and Technology, Tsukuba, Japan.

²Department of Environmental Science, Faculty of Science, Toho University, Funabashi, Japan.

³Civil Engineering Research Laboratory, Central Research Institute of Electric Power Industry, Abiko, Japan.

⁴Department of Earth and Planetary Science, Graduate School of Science, University of Tokyo, Tokyo, Japan.

⁵Department of Earth and Planetary Systems Science, Graduate School of Science, Hiroshima University, Higashi-Hiroshima, Japan.

facilitating creep [e.g., *Brune et al.*, 1969; *Zoback et al.*, 1987]. *Reinen et al.* [1991; 1992; 1994] conducted rotary shear sliding experiments on antigorite-, lizardite- and chrysotile-bearing serpentinites under room temperature conditions. *Reinen et al.* [1994] documented the weakness of chrysotile-bearing serpentinite (friction coefficient (μ) of ~ 0.2) and suggested that this might explain the weakness of the San Andreas fault. However, chrysotile at pressure-temperature (P-T) conditions corresponding to ~ 9 km depth exhibited a substantially higher μ value (~ 0.5) [*Moore et al.*, 1996]. This result was attributed to the removal of absorbed water from the chrysotile surface at higher temperatures [*Morrow et al.*, 2000]. The presence of water (more specifically the pore water pressure) in an impermeable serpentinite fault in a particular orientation within a regional stress field can strongly affect both fault strength and stability.

[5] The other issue related to the serpentine rheology is whether the dehydration of serpentine triggers the intermediate-depth earthquake in a subducting slab. A term, called “dehydration embrittlement” [*Raleigh and Paterson*, 1965], had been used to try to explain the mechanism of the intermediate-depth earthquake; a pore pressure increase caused by the dehydration in low-permeable serpentine reduces its failure strength. However, the Clapeyron slope is negative at more than 2 GPa, corresponding to the depth at which the intermediate-depth earthquakes occur (>50 km). Therefore, such a higher-pressure condition prohibits the pore pressure increase. Although there were many experimental studies to resolve that paradox, they produced contradictory results. *Jung et al.* [2004] observed that dehydration products, i.e., fine olivine, were generated within and adjacent to faults showing brittle failures under various antigorite-serpentine unstable P-T conditions. On the other hand, *Chernak and Hirth* [2010] reported a ductile, distributed deformation in their antigorite-serpentine specimen, even at its unstable P-T condition (1.5 GPa, 700°C). As shown by these studies, the rheology of serpentinite is quite complicated. Thus, it is difficult to pinpoint the role of serpentinite in fault behavior and/or earthquake occurrence at intermediate depths.

[6] Serpentine accompanied by high pore water pressure may play an important role in slow earthquakes and/or nonvolcanic tremors where a subducting plate contacts a serpentinized mantle wedge [e.g., *Kamiya and Kobayashi*, 2000; *Obara*, 2002]. For example, along the Nankai trough in southwestern Japan, a high- V_p/V_s region at 30–40 km depth [*Matsubara et al.*, 2009] has been implicated in short-term, slow-slip events and low-frequency nonvolcanic tremors at the junction of the subducting Philippine Sea plate and the serpentinized mantle wedge. These slow earthquakes and nonvolcanic tremors are kinds of brittle shear-slip phenomena since they generate seismic waves. However, the scaling law between duration and seismic moment for slow earthquakes was found to differ from that for regular earthquakes [*Ide et al.*, 2007]. *Ide et al.* [2007] also reported a $1/f$ decay in the source spectra of nonvolcanic tremors. *Ando et al.* [2010] suggested a model that could explain a cause of the $1/f$ decay. The model, involving unstable patches distributed in a stable sliding background, represented the fault heterogeneity of the sliding properties in a brittle-ductile transition regime. Experimental studies of these properties would be useful if we can find a P-T condition allowing for

heterogeneous sliding properties (e.g., brittle, frictional properties and creep-type properties) in serpentine rocks.

[7] Here, we sought to identify the mechanical factors that control deformation in serpentine. Our experimental testing machine used Ar gas for the confining pressure medium. This gas-pressure medium generally reduces the friction in the testing machine compared with Griggs-type rigs, allowing for detailed discussions of the deformation mechanisms shown by transient behaviors following a change in velocity (strain rate). This experimental study of the frictional properties of serpentine will help reveal the earthquake mechanisms relevant to serpentine-bearing faults, even though our system could not produce high pressure of the order of gigapascals.

2. Fundamentals of Frictional Behaviors Following Stepwise Changes in Slip Velocity

[8] The sliding behavior response to stepwise changes in sliding velocity in the brittle (friction) regime has been well studied for various rocks and minerals in order to understand the seismogenic process. Transient behavior during such deformations can be described as the combination of a direct effect and an evolutionary effect, called the “rate- and state-dependent friction constitutive law” (RSF law) [*Dieterich*, 1979, 1981]. The direct effect is an instantaneous response with a positive proportionality coefficient (a) to the change in magnitude of the velocity; the evolutionary effect is decay in the friction (b) toward the next frictional steady state, as the magnitude of the velocity changes. The velocity dependence of the friction (strengthening or weakening) is determined by whether $a - b$ is positive or negative. The RSF law is described as

$$\Delta\mu = a \ln\left(\frac{V}{V_0}\right) + b \ln\left(\frac{V_0\theta}{Dc}\right) \quad (1a)$$

$$\dot{\theta} = 1 - \frac{V\theta}{Dc}, \quad (\text{aging law}) \quad (1b)$$

where $\Delta\mu$ is the change in friction from a reference value μ_0 , V is the slip velocity, V_0 is the slip velocity before the stepwise change, θ is the state variable, and Dc is the characteristic distance [e.g., *Marone*, 1998]. Elastic deformation of the experimental system generally affects behavior, following

$$\frac{d\mu}{dt} = k(V_{lp} - V) \quad (2)$$

where V_{lp} is the velocity at the loading point and k (in inverse microns) is a normalized machine stiffness that the stiffness of the system normalized by normal load. To fit each parameter, equations (1) and (2) are solved simultaneously.

[9] The constitutive law was simplified by *Nakatani* [2001] as a relationship between velocity and stress,

$$V = V_0 \exp\left(\frac{\tau - \Phi}{a\sigma_n}\right) \quad (3)$$

According to this equation, the sliding velocity increases with increasing a difference between the applied shear stress τ and strength Φ , and with decreasing a . Therefore, the direct

effect a should be a control parameter that accelerates sliding. Moreover, the strength Φ , which corresponds to $\sigma_n[\mu_0 + b \ln(\theta/\theta_0)]$, depends on the real contact area [Dieterich and Kilgore, 1994; Nagata *et al.*, 2008]. If the real contact area no longer depends on the state (the healing time or the velocity), meaning that asperity cannot develop, Φ remains only a constant $\sigma_n\mu_0$. Two phenomena could produce this condition: The development of the contact area is maximized, or the velocity is greater than the “cutoff velocity.” Otherwise, sensitivity of the state b becomes 0 and Φ becomes constant $\sigma_n\mu_0$. In such cases, only the direct effect is present. Reinen *et al.* [1991, 1992, 1994] found two types of transient responses to stepwise changes in slip velocity: “state-variable-dominated behavior” at relatively high velocities (0.1–10 $\mu\text{m/s}$) and “flow-dominated behavior” at low velocities (less than 0.1 $\mu\text{m/s}$). These transient responses may contain information about how serpentinite accommodates deformation. Reinen *et al.* [1992, 1994] adapted the rate-strengthening constitutive law (first term of 1a) to depict viscous flow behavior (nonlinear):

$$\Delta\mu = a \ln\left(\frac{V}{V_0}\right) \quad (4)$$

The mechanical model under such a flow regime may resemble the viscoelastic model, combining equations (2) and (4).

[10] As described above, transient behavior that follows a stepwise change in velocity provides information about the mechanics of a fault zone and how the deformation mechanism is related to conditions. In this study, transient behaviors were related to experimental conditions, including slip velocity and temperature, and reflect the complex rheology of serpentinite.

3. Experimental Procedure

[11] The serpentinite block sampled from Oheyama (Kyoto, Japan) consisted predominantly of antigorite, with olivine, talc, and a small volume of iron oxide minerals in crack-sealing veins. Olivine and talc, which are products of dehydration, were removed so that the simulated gouge consisted of pure antigorite. The serpentinite block was crushed and antigorite aggregates were picked out. These aggregates were milled to a grain size of <200 μm . The average grain size was 1.7 μm , as measured by a laser particle-size analyzer, and 90% of the grains were <18.0 μm in diameter. Although the impurities present in the starting material were not detected in X-ray diffraction (XRD) analysis of the milled material (see Figure 10 in section 5), scanning electron microscopy (SEM) imaging showed that small amounts of iron oxide minerals and diopside were still present (see Figures 11–13 in section 5). The fluid flow properties of permeability and storage capacity were measured using the pore pressure oscillation method [e.g., Fischer and Paterson 1992; Takahashi *et al.*, 2007] at room temperature with 100 MPa of confining pressure and 30 MPa of pore pressure (distilled water). The permeability and the storage capacity of the gouge prior to shear were $6.24 \pm 0.56 \times 10^{-18} \text{ m}^2$ and $7.49 \pm 0.15 \times 10^{-4} \text{ MPa}$, respectively, and those after shear at 2.3 mm displacement were $3.64 \pm 0.37 \times 10^{-19} \text{ m}^2$ and $1.23 \pm 0.21 \times 10^{-4} \text{ MPa}$, respectively.

[12] The experimental apparatus for this study was a gas-medium, high-pressure, high-temperature triaxial testing machine at the National Institute of Advanced Industrial Science and Technology (AIST), Japan. The details of the set-up have been described by Masuda *et al.* [2002] and Takahashi *et al.* [2007, 2009]. The machine consisted of a cylindrical pressure vessel, a loading system, a pressure-generating system for confining pressure, and two servo-controlled pressure intensifiers capable of applying a maximum of 200 MPa for both confining pressure (P_c) and pore pressure (P_p). The confining pressure was provided by argon gas, and the pore pressure medium was distilled water. All experiments were carried out with $P_c = 100 \text{ MPa}$ and $P_p = 30 \text{ MPa}$.

[13] An axial load was applied with a constant axial-shortening velocity, which was measured by two force gauges. One force gauge was installed in the load actuator outside the pressure vessel (external load cell) and the other was attached to the side of the lower piston inside the pressure vessel (internal load cell in Figure 1a). Differential stress was calculated using measurements from the internal load cell. Axial displacement was measured with a linear variable differential transformer (LVDT) fitted to the load actuator. The cylindrical internal furnace (Figure 1a) consisted of upper and lower heating zones that could reach a maximum of 800°C [Masuda *et al.*, 2002]. Two thermocouples were inserted through holes in the upper and lower pistons to points just above and below the specimen assembly. The temperature data were then used as feedback for the independent operation of each thermocontroller. The gap between the furnace bore and the copper jacket above the hot zones was filled with a heat-insulating material to prevent convection of the argon gas. The temperature (T) was increased at a constant rate of 9.6°C/min. Once the temperature reached the target value, loading was initiated with a constant displacement velocity. During the experimental run, the difference between the upper and lower temperatures, as monitored by the thermocouples, was less than 5°C. Pressure measurements were accurate to 0.1 MPa for the rated capacity, and load measurements in the internal load cell were accurate to 1 kN for the rated capacity. The uncertainties produced an error of approximately ± 0.03 in the friction coefficient in the case of $(P_c, P_p) = (100 \text{ MPa}, 30 \text{ MPa})$. The friction coefficient (μ) is defined as the shear stress (τ) normalized by the effective normal stress (σ_n):

$$\mu = \frac{\tau}{\sigma_n} = \frac{\sigma_{\text{dif}} \cdot \sin(2\phi)}{2(\sigma_{\text{dif}} \cdot \sin^2(\phi) + P_c - P_p)}, \quad (5)$$

where σ_{dif} is the differential stress (i.e., the axial stress minus P_c) and ϕ is the angle of the oblique surfaces of the alumina blocks to the axis (i.e., 30°). The load cell data included the friction associated with deformation of the copper jacket and interfaces between pistons, alumina spacers, and tungsten carbide (WC) spacers. The friction at the copper jacket and these interfaces can affect apparent sample behaviors. To remove this friction, the strength of the copper jacket during deformation was measured (Figure 2) using greased Teflon sheets instead of gouge for lower-temperature cases ($\leq 250^\circ\text{C}$) at the same effective pressure condition (70 MPa). Weakening of the copper jacket accompanied increasing temperature but ceased toward $T = 250^\circ\text{C}$ (Figure 2). The friction of

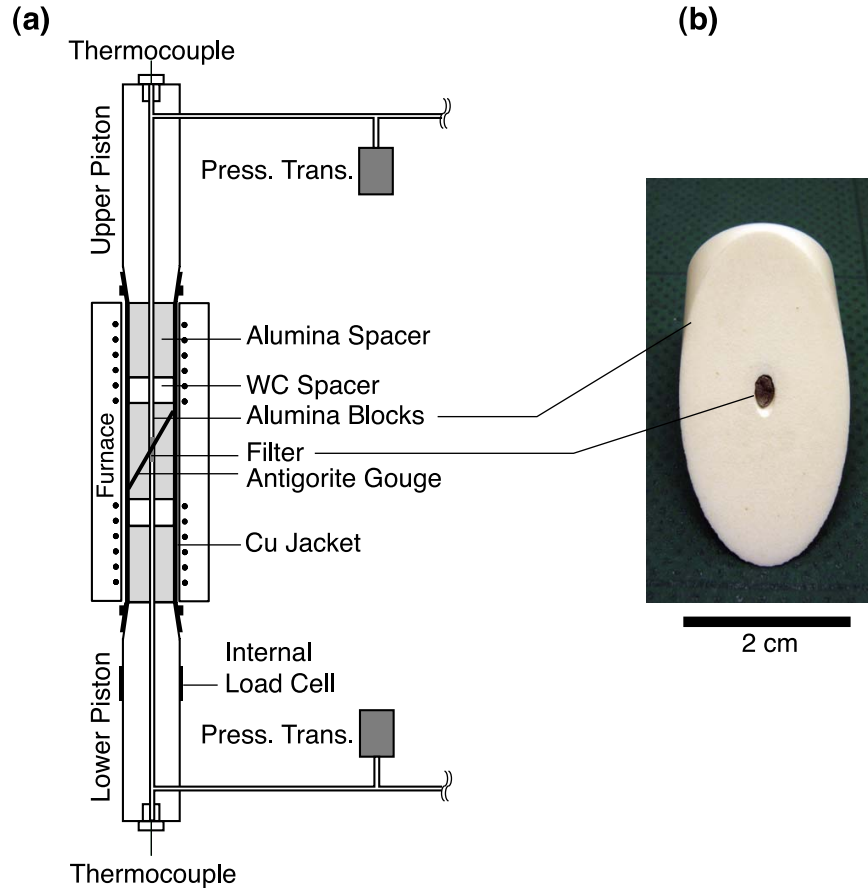


Figure 1. (a) Schematic configuration of the specimen-piston assembly. The assembly and furnace were placed in a pressure vessel. (b) Photograph of the oblique surface (30° to axis of the assembly) of alumina blocks (20 mm diameter, 40 mm long). A filter (piece of stainless steel mesh) was inserted into the central hole to impede gouge loss from the sliding layer to the pore water line.

the copper jacket became negligible at $T > 450^\circ\text{C}$ [Moore and Lockner, 2008]. We assumed that the friction of the copper jacket would decrease asymptotically until $T = 450^\circ\text{C}$, whereas the friction between the interfaces of the pistons would remain at higher temperatures. An empirical master curve for the deformation of the copper jacket is a function of temperature and displacement, d (in millimeters):

$$L_{cu} = C_1 + C_2 \cdot (T - 450)^2, (T < 450^\circ\text{C}), \quad (6a)$$

$$L_{cu} = C_1, (T \geq 450^\circ\text{C}), \quad (6b)$$

where $C_1 = (8.88d - 0.79d^2) \times 10^{-1}$, $C_2 = (1.40 + 1.28d - 0.22d^2) \times 10^{-5}$, and L_{cu} is the load (in kilonewtons) for copper jacket deformation. The effect of friction within the copper jacket can then be removed from the load data.

[14] The specimen assembly and spacers were placed into a 0.3 mm thick copper jacket. Sliding deformation was applied to a thin sample (~ 0.8 mm) of antigorite gouge (1.0 g) sandwiched between two alumina blocks (20 mm diameter, 40 mm long) with oblique surfaces oriented at 30° to the cylinder's axis. A stainless steel mesh sheet was installed in a hole in the pre-cut alumina block (Figure 1b) to impede extrusion of the gouge into the pore water. The sliding sur-

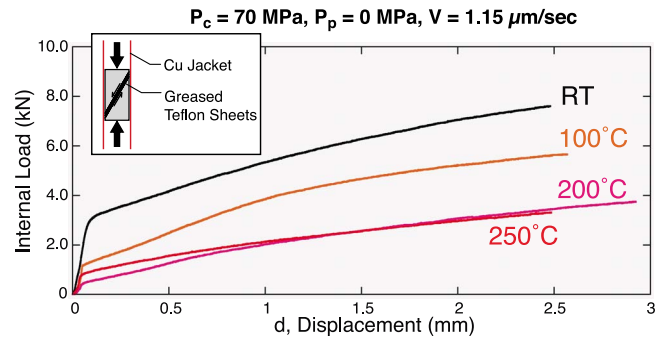


Figure 2. Axial loading of the copper jacket as a function of shear displacement d for temperatures from room temperature (RT) to 250°C under constant conditions of $(P_c, P_p, V) = (70 \text{ MPa}, 0 \text{ MPa}, 1.15 \mu\text{m/s})$. Shear was applied to greased Teflon sheets (four layers) to exclude friction. The copper strength at 250°C (almost at the thermal limit of the Teflon) was almost the same as that at 200°C . These results can be used to establish a master curve for copper jacket strength as a function of d and T (2) to remove the effect of copper jacket friction from the experimental data.

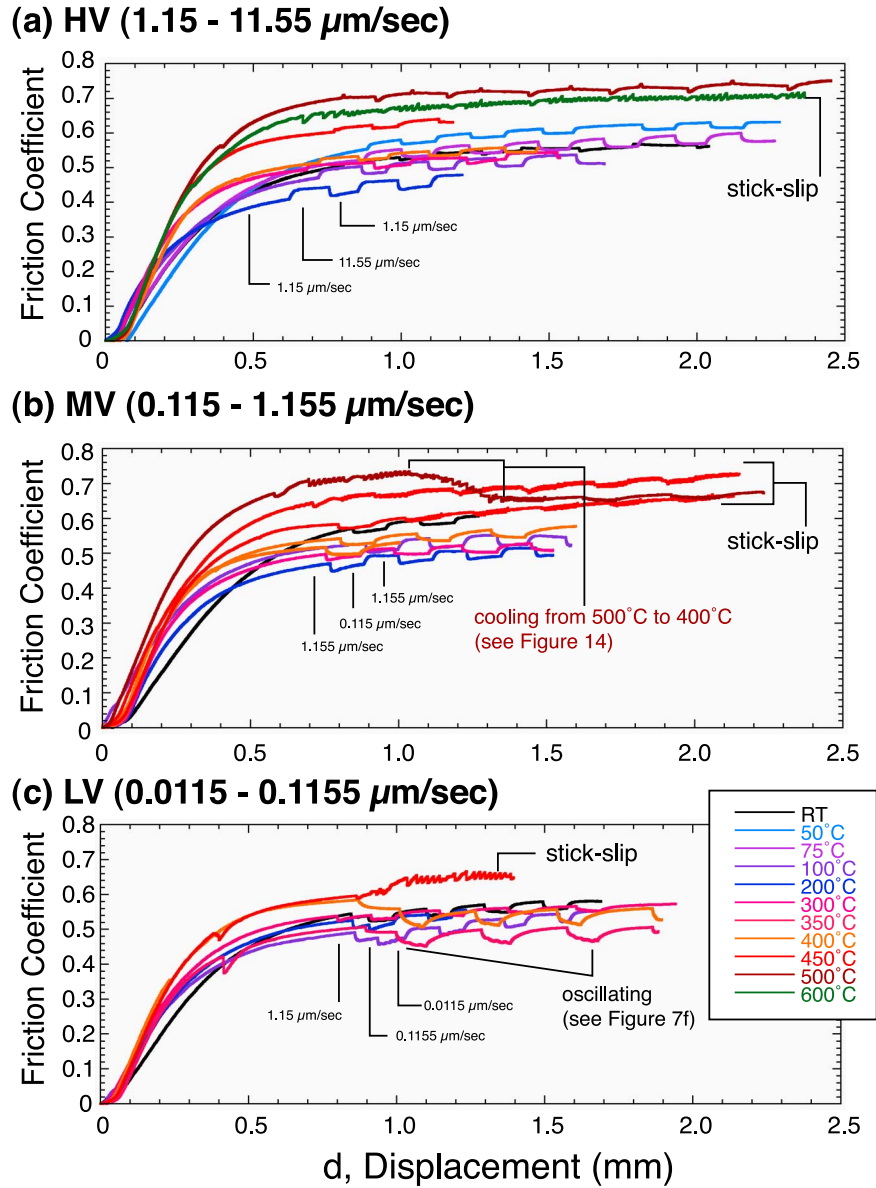


Figure 3. Friction coefficient as a function of displacement d for all experimental runs. Each color refers to a specific temperature. After initial elastic increases of the friction coefficient, stepwise changes in V were introduced in order to trigger transient responses. Three velocity conditions were prepared: alternation between (a) 1.15 and 11.55 $\mu\text{m/s}$ (HV), (b) 0.115 and 1.155 $\mu\text{m/s}$ (MV), and (c) 0.0115 and 0.1155 $\mu\text{m/s}$ (LV).

faces of the alumina blocks were ground with #80 silicon carbide abrasive. Prior to applying P_c and P_p , the vessel and the lines were evacuated for approximately 1 h.

[15] Axial loading by the hydraulically operated actuator produced shear deformation in the antigorite gouge between the oblique surfaces of the alumina blocks (Figure 1a). Deformation began with a constant shortening velocity of 1.0 $\mu\text{m/s}$, meaning a slip velocity of 1.15 $\mu\text{m/s}$ along the oblique surface. The axial-shortening velocity then changed abruptly at an axial displacement of 0.6–0.7 mm, where the initial increase of the elastic strength was almost complete. The axial-shortening velocity spanned 4 orders of magnitude, from 0.01 to 10 $\mu\text{m/s}$, which corresponds to slip velocities ranging from 0.0115 $\mu\text{m/s}$ to 11.5 $\mu\text{m/s}$ (from $\sim 1.4 \times 10^{-5}/\text{s}$ to $\sim 1.4 \times 10^{-2}/\text{s}$ in strain rate). Axial-displacement mea-

surements by the LVDT at the load actuator were accurate to 1 μm for the rated capacity, and the noise in the data was $\pm 0.3 \mu\text{m}$. Velocity was well constrained within an error of $\pm 0.2\%$.

4. Physical Properties of Antigorite Gouge

4.1. Strength and Velocity Dependence of the Antigorite Gouge

[16] Figure 3 presents the results of all experimental runs, plotting the friction coefficient against displacement. Deformation started with a constant slip velocity of 1.15 $\mu\text{m/s}$ until the initial rapid increase in friction was complete. At that first stage of sliding at 1.15 $\mu\text{m/s}$, the frictional strengths were scattered even under the same temperature conditions. This

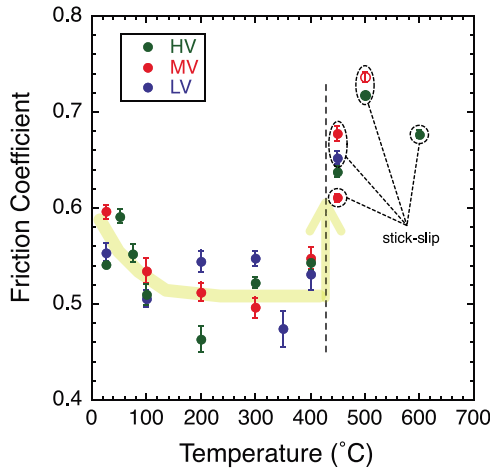


Figure 4. Friction coefficient as a function of T at $d = 1.2$ mm. Values for $(T, V) = (500^\circ\text{C}, \text{MV})$ were estimated using the general displacement-hardening trend. We plotted mean values between the friction at higher velocity and that at lower velocity. Errors indicated the differences. The dashed line indicates the boundary temperature across which the strength changes markedly. The strength gap was as much as 0.15 in terms of the friction coefficient.

scattering is attributable to the misalignment of precut alumina spacers in packing the gouge powder. Sliding velocity was then increased or decreased sharply by a factor of 10. Three sliding-velocity regimes were imposed: high-velocity (HV; Figure 3a) regime, alternating between 1.15 and 11.5 $\mu\text{m/s}$; medium-velocity (MV; Figure 3b) regime, alternating between 0.115 and 1.15 $\mu\text{m/s}$; and low-velocity (LV; Figure 3c) regime, alternating between 0.0115 and 0.115 $\mu\text{m/s}$. All runs showed ongoing displacement hardening.

[17] Stick-slip sliding was documented at $(T, V) = (600^\circ\text{C}, \text{HV})$; Figure 3a). Under lower-velocity conditions (MV and LV conditions), stick-slip sliding was observed at temperatures above 450°C (Figures 3b, 3c). The general level of friction also increased at these higher temperatures. Figure 4 plots the friction at around 1.2 mm of displacement against temperature. Each data point plotted in Figure 4 represents a mean level between the frictional strength at higher velocities and that at lower velocities during velocity step changes. The error bars show the differences. Gouge strength varied by approximately ~ 0.1 in terms of the friction coefficient at a certain temperature but tended to decrease until $T = 200^\circ\text{C}$. As the temperature was increased from 400°C to 450°C , gouge strength increased markedly by as much as ~ 0.15 in terms of the friction coefficient. The increase in the friction coefficient was quite significant in comparison with variations among the data.

4.2. Transient Response of Antigorite

4.2.1. Nonlinear Least Squares Curve Fitting

[18] All friction curves showed “displacement-hardening” trends (Figure 3), which need to be removed in order to calculate parameters in constitutive models. The hardening rate converged toward a “steady state” with increasing displacement. Each local linear trend in hardening h_i (Figure 5) was calculated between the two points at each end of the

velocity step under the same velocity conditions (Figure 5). The hardening rate of the local trend h_i was defined for a certain frictional behavior for each velocity step change. After detrending, curve fitting determined the parameters.

[19] Figure 6 shows typical transient responses for various temperatures under HV conditions, with curve-fitting results based on different models. Typical frictional behavior was exhibited at room temperature (Figure 6a). This behavior was modeled using RSF law (1) with two state variables obeying an “aging law,” as has been used in many previous experimental studies [e.g., *Reinen et al.*, 1994; *Blanpied et al.*, 1998], given by derivative forms as

$$\dot{V}_{body} = \frac{V_{body}}{a_1} \left[k_1 (V_{lp} - V_{body}) - b_i \frac{\dot{\theta}_i}{\theta_i} \right], \quad (7a)$$

$$\dot{\theta}_i = 1 - \frac{V_{body}\theta_i}{Dc_i}, \quad (7b)$$

$$\Delta\mu = k_1 (V_{lp} - V_{body}), \quad (7c)$$

where V_{body} is the velocity of the specimen and $i = 1, 2$. At temperatures between 50°C and 400°C , the evolution effect

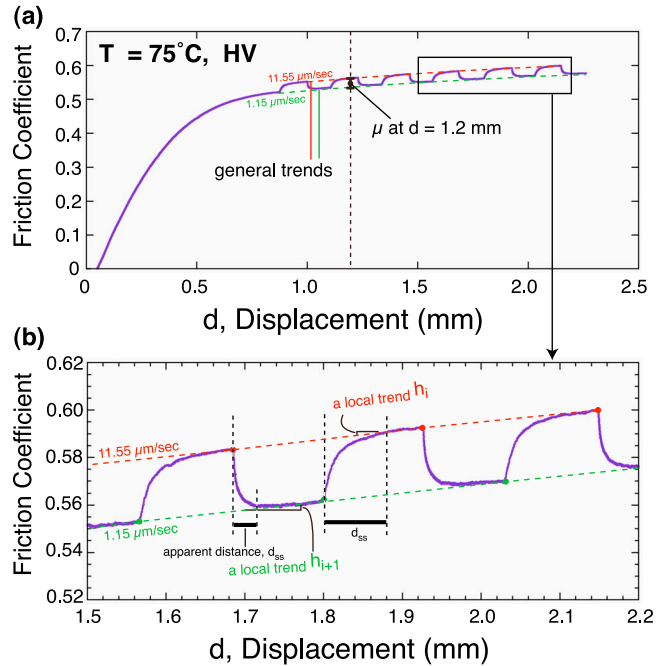


Figure 5. Method of evaluating the general displacement-hardening trend for each stepwise velocity change test. (a) Example for $(T, V) = (75^\circ\text{C}, \text{HV})$ showing the overall trend (red dashed line for $V = 11.55 \mu\text{m/s}$ and green dashed line for $V = 1.15 \mu\text{m/s}$). The overall hardening rates decreased with increasing d . (b) To remove the overall hardening trend from each transient response, the local trend h was determined as the slope between the two points at the end of each stepwise velocity change. Detrended data were used for curve fitting, as shown in Figures 6 and 7. The apparent distance under steady state friction for a positive velocity change was approximately twice as large as that for a negative velocity change (Appendix A).

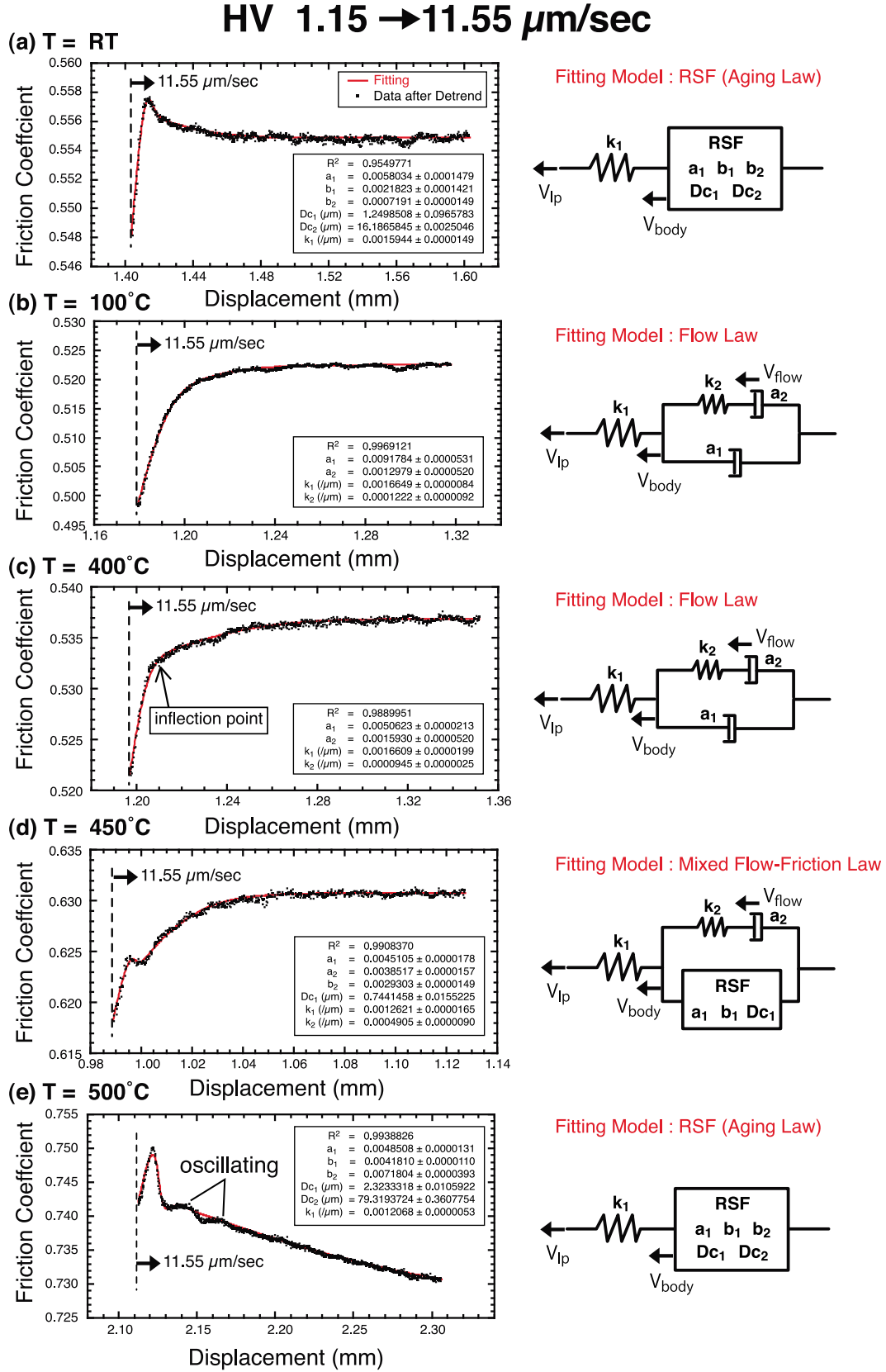


Figure 6

was not present (Figures 6b and 6c), and the specimen's behavior resembled "viscoelastic" behavior. The transient response at higher temperatures exhibited a distinct inflection point (arrow in Figure 6c) that divided the behavioral response into an initial, instantaneous response corresponding to the frictional constitutive law, a_1 , and a subsequent response, a_2 , that probably reflects viscoelastic flow behavior, as given by

$$\dot{V}_{flow} = \frac{k_2 V_{flow}}{a_2} (V_{body} - V_{flow}), \quad (8a)$$

$$\dot{V}_{body} = \frac{V_{body}}{a_1} [k_1 (V_{lp} - V_{body}) - k_2 (V_{body} - V_{flow})], \quad (8b)$$

$$\Delta \dot{\mu} = k_1 (V_{lp} - V_{body}), \quad (8c)$$

where V_{flow} is the flow velocity driven at an element marked as a viscous damper and k_1 is the normalized machine stiffness marked as a spring (see schematic in Figure 6c). Parameters a_2 and k_2 in the subsequent response resemble viscosity and normalized stiffness, respectively; this model is referred to as the "flow-law" model. Although behavior at 450°C appears to have been complex (Figure 6d), a combination of RSF and flow laws provided an adequate model. A slight decay in the friction response took place after the first peak, which implies that the evolution effect made a contribution at $T = 450^\circ\text{C}$ even though flow behavior had become dominant. The RSF law (with one state variable) and the flow law were connected in parallel (Figure 6d), a configuration that is referred to as the "mixed friction-flow law." Simultaneous equations with derivative forms were solved as follows:

$$\dot{V}_{flow} = \frac{k_2 V_{flow}}{a_2} (V_{body} - V_{flow}), \quad (9a)$$

$$\dot{V}_{body} = \frac{V_{body}}{a_1} \left[k_1 (V_{lp} - V_{body}) - k_2 (V_{body} - V_{flow}) - b_1 \frac{\dot{\theta}_1}{\theta_1} \right], \quad (9b)$$

$$\dot{\theta}_1 = 1 - \frac{V_{body} \theta_1}{Dc_1}, \quad (9c)$$

$$\Delta \dot{\mu} = k_1 (V_{lp} - V_{body}). \quad (9d)$$

At 500°C (Figure 6e), frictional transient behavior reappeared, demonstrating the evolution effect. Those simultaneous equations (7)–(9) were used to obtain a best fit curve and optimal parameters.

[20] After deciding which model should be used for curve fitting, optimum values of the parameters in each model were sought using iterative least squares inversion [Reinen and Weeks, 1993; Noda and Shimamoto, 2009]. The Runge-Kutta method was used with a set of simultaneous derivative equations, (7)–(9), to create and validate the frictional curve during the iterative process. The variables in the above equations, $\Delta \mu$, V_{body} , V_{flow} , and/or θ_i , were assumed to be 0, V_0 , V_0 , and/or Dc_i/V_0 , respectively, at the beginning of each stepwise change in velocity.

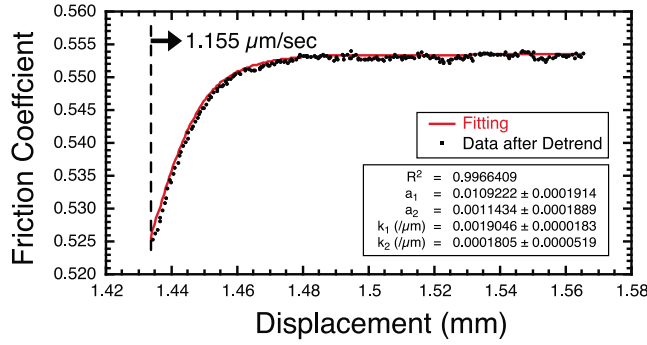
[21] The normalized machine stiffness k_1 was treated as an uncertain parameter in this study. It was difficult to determine the elastic constant of the machine directly under high-temperature conditions because the temperature distribution along the piston and around the O-rings varied from one run to the next. The normalized machine stiffness k_1 was assumed to be the optimum value, which was obtained using the Levenberg-Marquardt method as described by Noda and Shimamoto [2009]. A uniform weight function was used owing to uncertainty in the normalized stiffness k_1 that affects the data associated with the instantaneous response. The least squares was resolved using Matlab with the Optimization Toolbox (MathWorks®). The iterative least squares inversion method was not able to reproduce the optimized curve within applicable errors for stick-slip or oscillating behavior (Figure 6e). For each graph in Figures 6 and 7, a set of optimum values and the errors (standard deviation, 1σ) associated with the parameters were established. The optimized parameters, errors, and correlation matrices for Figures 6 and 7 are summarized in Table 1.

[22] As a technical note regarding the transient responses and curve fitting, we point out that the transient response at a negative velocity step was apparently simpler than that at a positive velocity step (see, for example, Figure 5 and Figure A1 in Appendix A), even though we applied the same model (Appendix A). Thus, it is difficult to recognize inflection points in the friction curves of complex models at negative velocity steps, even when using simulated data containing no noise. Transient responses written by complex models, such as the RSF law with double evolution effects (equation (7)) and/or the flow law with a direct effect and a spring damper in the specimen (equation (8)), tend to be concealed by an effect of the spring of the system (expressed by the normalized stiffness, k_1) at stepwise reduction in velocity. Either curve fitting using complex models for the real cases at the negative velocity step that had a certain level of noise tended to be unsuccessful, or the optimized parameters did not have adequate confidence (see Appendix A). For this reason, discussion of the relationships between the parameters and deformation conditions is limited to those for stepwise increases in velocity. On the other hand, the total change in friction at steady state $\Delta \mu_{ss}$, which does not

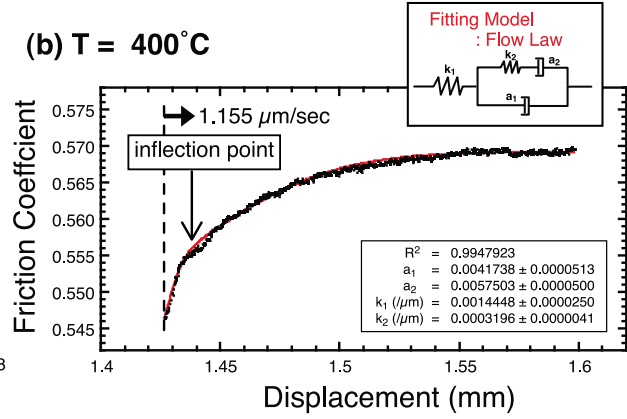
Figure 6. Change in friction coefficient (left-hand side) for $V = \text{HV}$ condition (positive change in V from 1.15 to 11.55 $\mu\text{m/s}$) and the possible constitutive models (fitting models) that might explain such behaviors (right-hand side) for various temperatures. (a) At room temperature (RT), the behavior was typical frictional behavior expressed by RSF law (7). At (b) 100°C and (c) 400°C, a fitting law that has a spring damper in the specimen body (flow law) is appropriate. (d) At 450°C, the best model was a "mixed flow-friction law," combining flow and RSF laws. These possible constitutive models with optimized parameters (red curves) correlated well with the data. Each set of optimized parameters and errors (1σ) is noted in a box. (e) At 500°C, oscillation that is due to $a_1 - b_1 \sim 0$ caused failure of the model fit, although the behavior was essentially frictional.

MV

(a) $T = 100^\circ\text{C}$

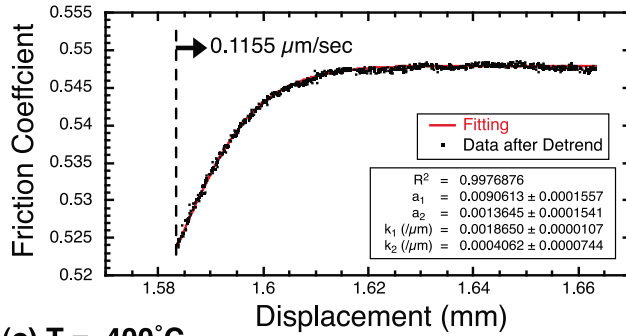


(b) $T = 400^\circ\text{C}$

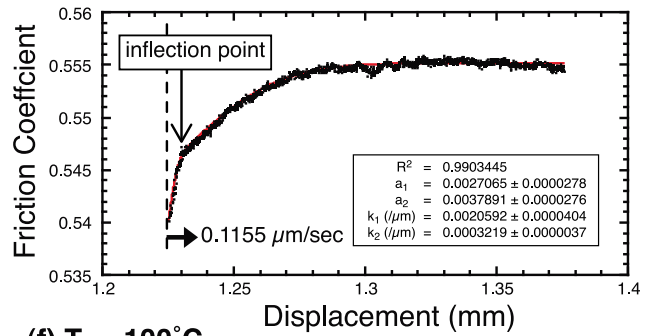


LV

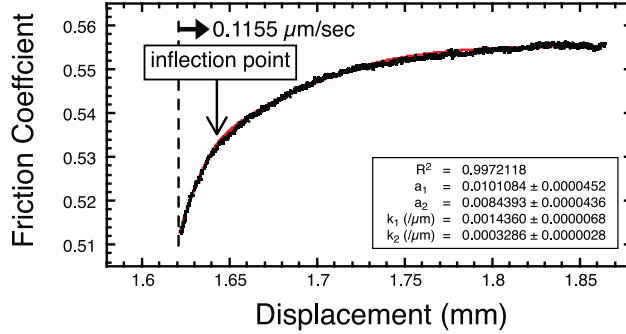
(c) $T = 100^\circ\text{C}$



(d) $T = 300^\circ\text{C}$



(e) $T = 400^\circ\text{C}$



(f) $T = 100^\circ\text{C}$

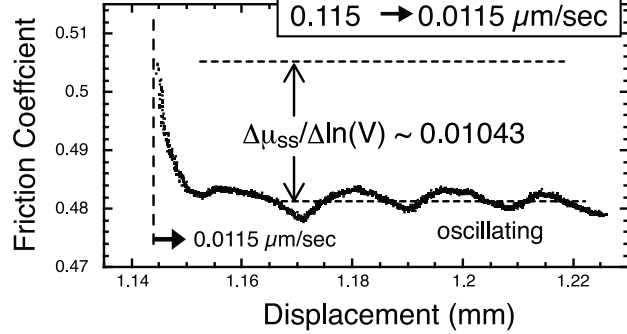


Figure 7. Plots of change in friction coefficient (a, b) for $V = MV$ (stepwise increase in V from 0.115 to 1.155 $\mu\text{m/s}$) and (c–e) at $V = LV$ (stepwise increase in V from 0.115 to 1.15 $\mu\text{m/s}$). The flow law was used for curve fitting in Figures 7a–7e. With increasing T , the inflection point became distinct because a_2 increased relative to a_1 . (f) Example of stepwise decrease of V from 0.115 to 0.0115 $\mu\text{m/s}$ at $T = 100^\circ\text{C}$. Continuous oscillations developed in several of the results for LV conditions (Figure 3c).

depend on transient responses, can be discussed for both cases of stepwise changes in velocity.

4.2.2. Results of Curve Fitting

[23] Under HV conditions (Figure 6), responses to stepwise velocity changes were a function of temperature: Frictional behavior prevailed at room temperature, flow behavior prevailed at 50°C to 400°C , friction-flow mixed behavior prevailed at 450°C , and frictional behavior prevailed at temperatures above 500°C . As the temperature was increased above 450°C , the evolution effect became apparent. At 600°C , stick-slip behavior became apparent (Figure 3a), which implies velocity weakening. Under lower-velocity conditions (MV

and LV conditions in Figure 7), all transient responses at stepwise increases in velocity were of the “flow” type, except at 450°C , where stick-slip behavior was evident (Figures 3b and 3c). At the lowest velocity (0.0115 $\mu\text{m/s}$), the transient response after a stepwise decrease in the velocity from 0.1155 $\mu\text{m/s}$ was oscillation at wavelengths of ~ 15 – $30 \mu\text{m}$ at several temperatures (Figure 3c and detail in Figure 7f). This observed oscillation did not represent the unstable sliding behavior (stick-slip) expressed by the one-body spring-block model with RSF law because the velocity dependence was positive. Additionally, the general behavior was of the flow type at the lowest velocity (Figure 7f). This oscillation may

Table 1. Results of The Optimization

Figure	Velocity	T (°C)	Transient Response: RSF Parameters	Result of Optimization: $R^2 = 0.9549771$ Optimized Values	Error (1σ)	Correlation Matrix ^a					
						a_1	b_1	b_2	Dc_1	k_1	
Figure 6a	HV	25	a_1 b_1 b_2 Dc_1 (μm) Dc_2 (μm) k_1 (1/μm)	0.0058034 0.0021823 0.0007191 1.2498508 16.1865845 0.0015944	0.0001480 0.0001421 0.0000149 0.0965783 0.0025046 0.0000149	1.0000000	0.9962343 1.0000000	0.4049262 0.3265196 1.0000000	-0.9492912 -0.9352023 -0.4874287 1.0000000	-0.9961195 -0.9849722 -0.4838216 0.9554295 1.0000000 1.0000000	k_1
Figure 4b	HV	100	a_1 a_2 k_1 (1/μm) k_2 (1/μm)	0.0091784 0.0012979 0.0016649 0.0001222	0.0000531 0.0000520 0.0000084 0.0000092	1.0000000	-0.9892223 1.0000000	-0.7148727 0.7163926 1.0000000	-0.9533322 0.9267480 0.6100620 1.0000000		
Figure 6c	HV	400	a_1 a_2 k_1 (1/μm) k_2 (1/μm)	0.0050623 0.0015930 0.0016609 0.0000945	0.0000213 0.0000199 0.0000129 0.0000025	1.0000000	-0.9180767 1.0000000	-0.2803221 0.2346495 1.0000000	-0.8411208 0.6896644 0.0183679 1.0000000		
Figure 6d	HV	450	a_1 a_2 b_1 Dc_1 (μm) k_1 (1/μm) k_2 (1/μm)	0.0045105 0.0038517 0.0029303 0.7441458 0.0012621 0.0004905	0.0000179 0.0000157 0.0000029 0.0155225 0.0000165 0.0000090	1.0000000	-0.9072287 1.0000000	0.0923616 0.1749704 1.0000000	0.8525227 -0.9862453 -0.3349736 -0.3887469 1.0000000	-0.9088801 0.8689555 0.0769625 0.2961463 -0.8444132 1.0000000	k_2
Figure ^b	Velocity	T (°C)	Transient Response: RSF Parameters	Result of Optimization: $R^2 = 0.9938826$ Optimized Values	Error (1σ)	Correlation Matrix ^a					k_1
Figure 6e	HV	500	a_1 b_1 b_2 Dc_1 (μm) Dc_2 (μm) k_1 (1/μm)	0.0048508 0.0041810 0.0071805 2.3233318 79.3193724 0.0012068	0.0000131 0.0000110 0.0000393 0.0105922 0.3607754 0.0000053	1.0000000	0.7004730 1.0000000	0.5822496 0.0424014 1.0000000	-0.4969594 -0.1895949 -0.8886208 1.0000000 1.0000000	0.4949554 0.1879699 0.8882729 -0.9999971 1.0000000	0.2454629 0.0421091 0.6494983 -0.7899896 0.7899796 1.0000000

Table 1. (continued)

Figure	Velocity	T (°C)	Transient Response: Flow Parameters	Result of Optimization: $R^2 = 0.9966409$ Optimized Values	Error (1 σ)	Correlation Matrix ^a			
			a_1 a_2 k_1 (μm) k_2 (μm)			a_1	a_2	k_1	k_2
Figure 7a	MV	100		0.0109222 0.0011435 0.0019046 0.0001805	0.0001914 0.0001889 0.0000183 0.0000519	1.0000000	-0.9975411 1.0000000	-0.7945215 0.7963652 1.0000000 1.0000000	-0.9696959 0.9620492 0.7034442 1.0000000
Figure 7b	MV	400		0.0041738 0.0057503 0.0014448 0.0003197	0.0000513 0.0000500 0.0000250 0.0000041	1.0000000	-0.9767490 1.0000000	-0.7595353 0.7639926 1.0000000 1.0000000	-0.7677986 0.6931250 0.2585965 1.0000000
Figure 7c	LV	100		0.0090613 0.0013645 0.0018650 0.0004062	0.0001557 0.0001541 0.0000107 0.0000744	1.0000000	-0.9990818 1.0000000	-0.8586149 0.8606230 1.0000000 1.0000000	-0.9777909 0.9737627 0.7720798 1.0000000
Figure 7d	LV	300		0.0027065 0.0037892 0.0020593 0.0003219	0.0000278 0.0000276 0.0000404 0.0000037	1.0000000	-0.9848149 1.0000000	-0.6880281 0.6905280 1.0000000 1.0000000	-0.7662396 0.7215416 0.1767740 1.0000000
Figure 7e	LV	400		0.0101084 0.0084393 0.0014360 0.0003286	0.0000452 0.0000436 0.0000068 0.0000028	1.0000000	-0.9760197 1.0000000	-0.7622725 0.7664981 1.0000000 1.0000000	-0.8788511 0.8086712 0.4604890 1.0000000

^a**Bold style:** higher absolute correlation than **0.8**.^bComplete optimization failed because of oscillation behaviors.

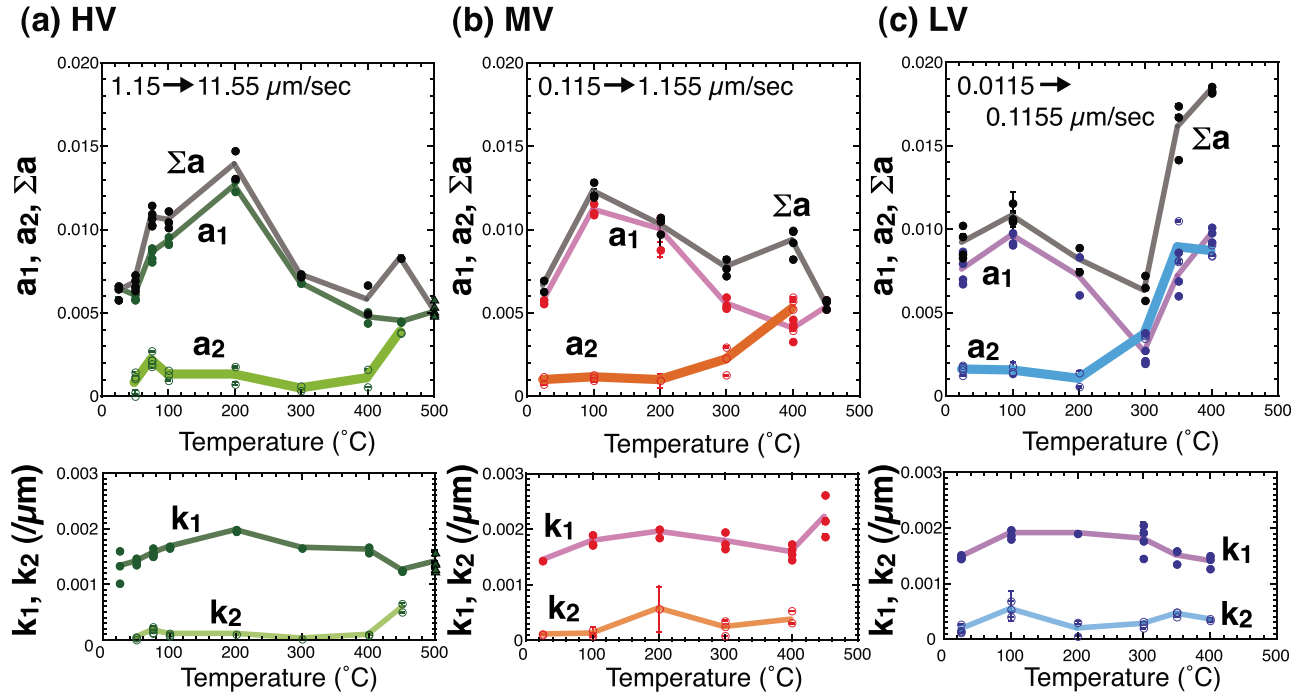


Figure 8. Parameters a_1 , a_2 , and Σa (upper) and k_1 and k_2 (lower) as functions of temperature for each velocity condition: (a) HV, (b) MV, and (c) LV. Lines in the graphs pass through the average values (Table 2). Parameter a_1 , the frictional parameter that expresses the direct effect, showed an obvious, complicated change with temperature. In contrast, parameter a_2 in the flow law increased with increasing T and with decreasing V . Both k_1 and k_2 showed no clear dependence on temperature.

be one of the characteristics of granular flow at lower sliding velocities. Such an oscillation at lower strain rates has also been observed in numerous studies of granular flow [Hatano, 2011]. Cluster aggregations of gouge particles might increase in size under a lower shear-strain rate, inducing strong heterogeneity in the sliding velocity in the simulated gouge zone (T. Hatano, personal communication, 2010).

[24] Regardless of the velocity conditions, inflection points became distinct at higher temperatures for the temperature range characterized by flow behavior. For example, comparing Figure 6b with 6c, Figure 7a with 7b, and Figure 7c with 7d, the parameter a_2 was larger at higher temperatures. Figure 8 presents values of the optimized parameters a_1 , a_2 , k_1 , and k_2 for different temperatures. Some values of normalized machine stiffness k_1 for the same T and V conditions were scattered, whereas others were well constrained. In general, k_1 did not exhibit a clear dependence on temperature and velocity. The normalized stiffness of the specimen k_2 was almost 1 order of magnitude smaller than k_1 , and there was no correlation between k_2 and T , V conditions. The average values of parameters a_1 , a_2 , b_1 , b_2 , Dc_1 , Dc_2 , k_1 , and k_2 are summarized in Table 2.

[25] Parameters a_1 and a_2 varied, depending on T , V conditions. Parameter a_1 , the instantaneous response in the direct effect, demonstrated very complicated responses as a function of temperature. Comparing the features under HV conditions with those under LV conditions, temperature, which had both maximum and minimum values of a_1 , shifted downward by as much as 100°C through 2 orders of magnitude of velocity reduction.

[26] The increase in a_2 initiated at a lower temperature and also was greater at lower velocity. Temperature, which had begun to increase markedly at a_2 , then decreased by as much as 100°C, from 400°C under HV conditions to 300°C under LV conditions. This phenomenon may imply that viscous damping within the specimen body was accomplished by a thermally activated process because parameter a_2 increased with increasing temperature and with decreasing velocity.

[27] The velocity dependence of friction at steady state $\Delta\mu_{ss}/\Delta\ln(V)$, as a function of temperature (Figure 9), closely resembled the $\Sigma a (=a_1+a_2)$ of Figure 8, except for the contribution from evolution effects and instances of stick-slip. For the cases of stick-slip, $\Delta\mu_{ss}$ was defined as the difference between mean values of μ in stick-slip and μ_0 , using detrended data. The error of $\Delta\mu_{ss}/\Delta\ln(V)$ in stick-slip cases is represented by the amplitude of stick-slip per $\Delta\ln(V)$ in Figure 9. The velocity dependence $\Delta\mu_{ss}/\Delta\ln(V)$ for each velocity condition was positive until the temperature reached 450°C (for HV conditions; Figure 9a) or 400°C (for MV and LV conditions; Figures 9b and 9c). There appears to have been a mechanical transition from ductile (flow behavior) to brittle (friction behavior) processes at around 450°C. For LV conditions (Figure 9c), the decrease from positive $\Delta\mu_{ss}/\Delta\ln(V)$ at 400°C and negative $\Delta\mu_{ss}/\Delta\ln(V)$ at 450°C was sharp because of the largest Σa at 400°C under LV conditions.

5. Dehydration at Higher Temperatures

[28] Both the general strength and the transient responses changed radically at around 450°C. The average strength at 1.2 mm of displacement (Figure 4) increased markedly by as

Table 2. The Averages of the Parameters for Positive Velocity Step Changes

Velocity	T (°C)	Transient Response	a_1	a_2	b_1	b_2	Dc_1 (μm)	Dc_2 (μm)	k_1 (μm)	k_2 (μm)	$\Delta\mu_{ss}/\Delta\ln(V)$ at Positive V Step Change Test	Remarks
HV	25	RSF	0.00630 \pm 0.00041	—	0.00279 \pm 0.00062	0.00106 \pm 0.00048	1.01715 \pm 0.27600	19.37852 \pm 4.10993	0.00132 \pm 0.00028	—	0.00243 \pm 0.00044	
	50	Flow	0.00603 \pm 0.00038	0.00079 \pm 0.00072	—	—	—	—	0.00140 \pm 0.00006	0.00003 \pm 0.00002	0.00682 \pm 0.00048	
	75	Flow	0.00856 \pm 0.00033	0.00215 \pm 0.00047	—	—	—	—	0.00156 \pm 0.00008	0.00018 \pm 0.00006	0.01071 \pm 0.00061	
	100	Flow	0.00930 \pm 0.00022	0.00127 \pm 0.0003	—	—	—	—	0.00167 \pm 0.00001	0.00010 \pm 0.00002	0.01056 \pm 0.00051	
	200	Flow	0.01262 \pm 0.00032	0.00126 \pm 0.00051	—	—	—	—	0.00198 \pm 0.00002	0.00010 \pm 0.00000	0.01387 \pm 0.00083	
	300	Flow	0.00681 \pm 0.00005	0.00046 \pm 0.00014	—	—	—	—	0.00165 \pm 0.00000	0.00002 \pm 0.00000	0.00727 \pm 0.00009	
	400	Flow	0.00473 \pm 0.00033	0.00107 \pm 0.00052	—	—	—	—	0.00162 \pm 0.00004	0.00009 \pm 0.00001	0.00581 \pm 0.00085	
	450	Mixed	0.00449 \pm 0.00002	0.00381 \pm 0.00002	0.00343 \pm 0.00049	—	1.22339 \pm 0.47425	—	0.00125 \pm 0.00001	0.00057 \pm 0.00008	0.00488 \pm 0.00050	^a
	500	RSF	0.00509 \pm 0.00026	—	0.00473 \pm 0.00019	0.00092 \pm 0.00059	2.37743 \pm 0.26282	42.22370 \pm 12.89010	0.00140 \pm 0.00017	—	-0.00556 \pm 0.00024	^b
	600	Stick-Slip	—	—	—	—	—	—	—	—	-0.00155 \pm 0.00230	^c
MV	25	Flow	0.00565 \pm 0.00011	0.00096 \pm 0.00024	—	—	—	—	0.00143 \pm 0.0000	0.00011 \pm 0.00000	0.00661 \pm 0.00035	
	100	Flow	0.01116 \pm 0.00031	0.00112 \pm 0.00018	—	—	—	—	0.00179 \pm 0.00009	0.00012 \pm 0.00005	0.01228 \pm 0.00045	
	200	Flow	0.01000 \pm 0.00096	0.00093 \pm —	—	—	—	—	0.00194 \pm 0.00008	0.00056 \pm —	0.01031 \pm 0.00050	
	300	Flow	0.00556 \pm 0.00032	0.00216 \pm 0.00084	—	—	—	—	0.00178 \pm 0.00015	0.00023 \pm 0.00013	0.00772 \pm 0.00052	
	400	Flow	0.00409 \pm 0.00066	0.00522 \pm 0.00098	—	—	—	—	0.00159 \pm 0.00014	0.00037 \pm 0.00038	0.00932 \pm 0.00084	^a
	450	Mixed	0.00173 \pm 0.00217	0.00212 \pm 0.00163	0.00404 \pm 0.00240	—	0.46681 \pm 0.07224	—	0.00191 \pm 0.00013	0.00020 \pm 0.00020	0.00255 \pm 0.00185	^c
	500	Stick-Slip	—	—	—	—	—	—	—	—	0.00134 \pm 0.00045	^c
	500	Stick-Slip	—	—	—	—	—	—	—	—	-0.00303 \pm —	
	25	Flow	0.00758 \pm 0.00097	0.00157 \pm 0.00029	—	—	—	—	0.00147 \pm 0.00004	0.00017 \pm 0.00007	0.00915 \pm 0.00097	
	100	Flow	0.00963 \pm 0.00072	0.00152 \pm 0.00021	—	—	—	—	0.00190 \pm 0.00008	0.00054 \pm 0.00014	0.01078 \pm 0.00058	
LV	200	Flow	0.00719 \pm 0.00115	0.00099 \pm 0.00043	—	—	—	—	0.00190 \pm 0.00000	0.00018 \pm 0.00012	0.00818 \pm 0.00073	
	300	Flow	0.00263 \pm 0.00091	0.00366 \pm 0.00016	—	—	—	—	0.00180 \pm 0.00030	0.00026 \pm 0.00006	0.00629 \pm 0.00076	
	350	Flow	0.00718 \pm 0.00132	0.00891 \pm 0.00121	—	—	—	—	0.00151 \pm 0.00012	0.00045 \pm 0.00004	0.01609 \pm 0.00162	
	400	Flow	0.00970 \pm 0.00044	0.00865 \pm 0.00033	—	—	—	—	0.00140 \pm 0.00011	0.00036 \pm 0.00002	0.01835 \pm 0.00018	
	450	Stick-Slip	—	—	—	—	—	—	—	—	-0.00227 \pm 0.00175	^c
	450	Stick-Slip	—	—	—	—	—	—	—	—	—	

^aThe term “mixed” means “mixed flow-friction behavior,” as shown in Figure 6d.^bComplete optimization failure was caused by oscillation behaviors, as shown in Figure 6c.^cFor the cases of stick-slip, we could not find optimized results. Here, $\Delta\mu_{ss}$ was determined as a difference between mean values of μ in stick-slip and μ_0 .

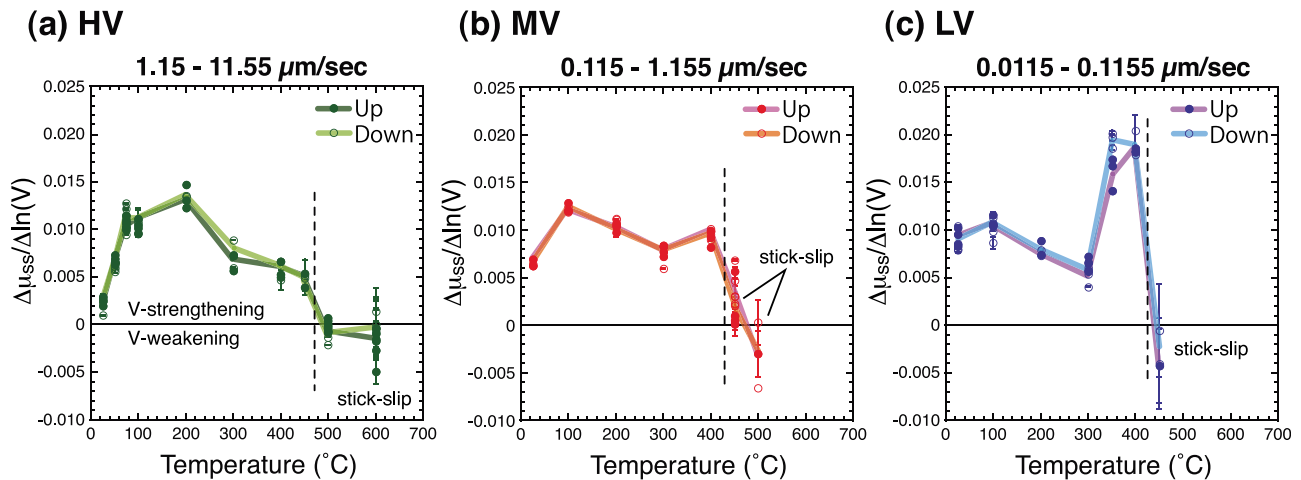


Figure 9. Velocity dependence of the friction coefficient as a function of temperature for each velocity condition: (a) HV, (b) MV, and (c) LV. $\Delta\mu_{ss}/\Delta \ln(V)$ for positive (solid circles) and negative (open circles) velocity changes became negative at ~ 450 to 500°C (dashed lines). Colored lines in the graphs pass through the average values (Table 2). Dashed lines indicate the boundary between flow and frictional behaviors.

much as ~ 0.15 (friction coefficient) between 400°C and 450°C . Transient responses to stepwise changes in velocity also reflected radically different deformation styles, from flow-type behavior at temperatures below 400°C to frictional behavior at temperatures above 450°C (Figures 6 and 7). Under HV conditions, the transient response was a gradual change in the deformation style, from mixed flow-friction behavior at 450°C to stick-slip behavior at 600°C . Regardless of the velocity conditions, the transient responses shifted to frictional behavior, including the evolution effect or stick-slip behavior above 450°C . Dehydration of antigorite takes place at $\sim 450^\circ\text{C}$ under $P_{\text{H}_2\text{O}} = 30 \text{ MPa}$ [Evans *et al.*, 1976]. It is conceivable that the drastic changes in physical properties were due to the dehydration of antigorite. Powder XRD of the experimental products showed evidence of dehydration, and SEM examinations identified the points in the deformed microstructure at which the dehydration reaction took place.

5.1. XRD Analysis of Experimental Products

[29] The XRD spectra for experimental products of HV conditions (Figure 10a) show conspicuous peaks associated with antigorite, but those for higher temperatures (600°C ; Figure 10b) also have peaks corresponding to forsterite (120) and (031) and talc (001), indicating that dehydration had commenced. New, weak peaks at $2\theta = 22.9^\circ$ and 32.3° , corresponding to forsterite (120) and (031), respectively, developed at 500°C . The XRD spectra for temperatures below 450°C under HV conditions do not exhibit any peaks corresponding to forsterite or talc. Spectra for 450°C under MV and LV conditions exhibit weak forsterite peaks (Figures 10c and 10d). This limited dehydration to form forsterite and talc may have caused drastic changes in the physical properties of the serpentine gouge, as discussed below.

5.2. Scanning Electron Microscopy

[30] The XRD spectra retained clear antigorite peaks even after dehydration had begun (Figure 10a). The intensities of the forsterite peaks in the XRD spectra were fairly weak,

even for $T = 600^\circ\text{C}$, indicating that only a limited amount of serpentine was involved in the dehydration reaction. Olivine is harder than serpentine, and it is generally the weaker minerals in a gouge (e.g., antigorite) that control its strength and frictional properties [e.g., Logan and Rauenzahn, 1987; Kawamoto and Shimamoto, 1998; Takahashi *et al.*, 2007; Collettini *et al.*, 2009; Moore and Lockner, 2011].

[31] Figures 11–13 are photographs of backscattered-electron SEM images of experimental products. These Riedel shears, mainly R1 and P shears at lower temperature (Figure 11), surrounded the relatively large antigorite grains, resulting in shear-aligned networks. Shear networks were also present in the higher-temperature material (MV, 450°C ; Figure 12), but comminuted material consisting of $<500 \text{ nm}$ grains with a bright backscatter pattern was also present in the Riedel shears (Figure 12c) and between the relatively larger antigorite grains (Figures 12d–12f). Using an energy-dispersion spectrometer (EDS) of SEM, the bright particles were identified as forsterite. They were present only in shear-localized zones; nearby areas of aggregated fine antigorite grains exhibited no forsterite (Figure 12g). Streaky alignments of forsterite particles were well developed along some R1 shears (LV, 450°C ; Figure 13), and some of the aligned forsterite retained the original orientation of the antigorite cleavages (Figure 13c).

[32] Both the XRD spectra and SEM images for the experimental products at $T \geq 450^\circ\text{C}$ (except one case at $(T, V) = (450^\circ\text{C}, \text{HV})$) indicate that only a limited amount of the serpentine was involved in the reaction. In spite of the low proportion of forsterite in these examples, more significant amounts of fine-grained, aligned forsterite were locally present in the shear-localized zones, where they contributed to strengthening and caused the gouge behavior to be of the friction type. Serpentine in shear-localized zones was preferentially altered to forsterite, suggesting shear-induced dehydration. These results are of great importance to understanding the development of the physical properties of faults having hydrous minerals during metamorphism. These SEM observations were also similar to previous results of Jung

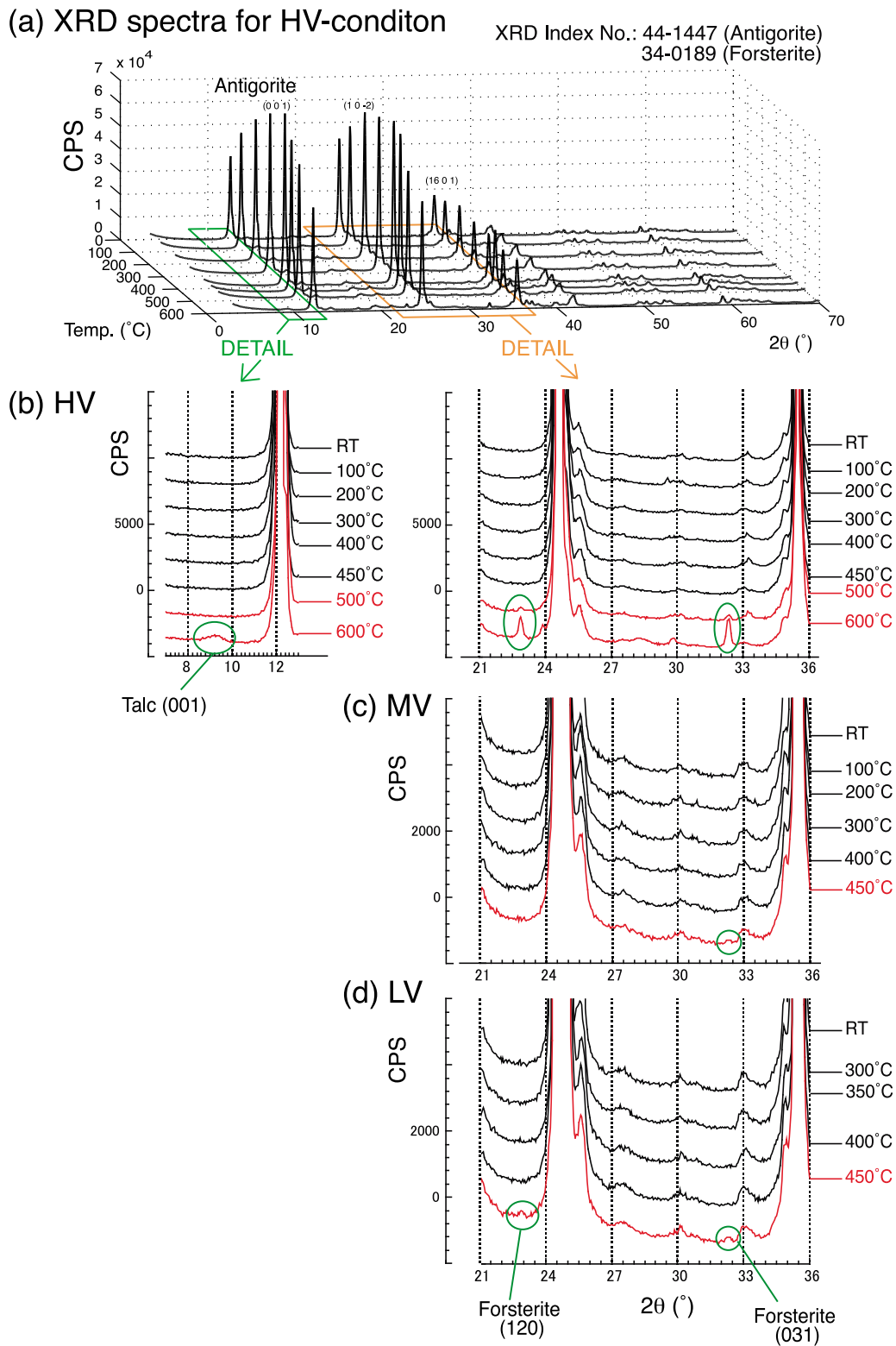
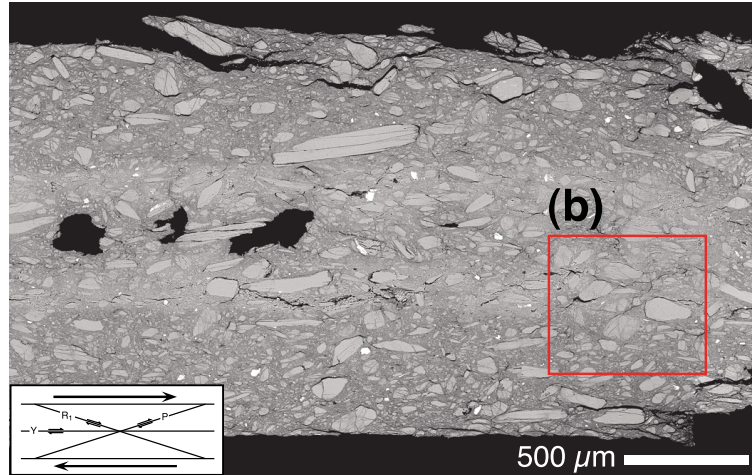
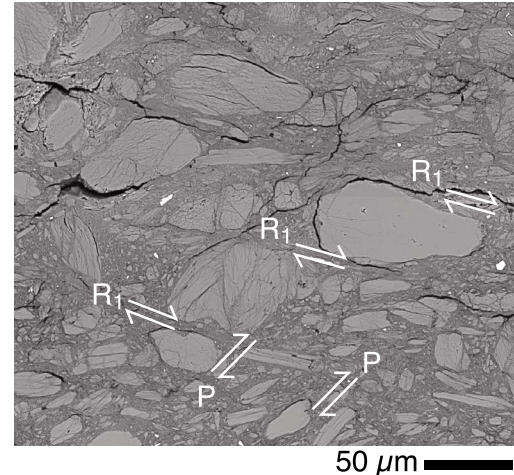


Figure 10. XRD spectra for randomly oriented experimental products of antigorite gouge, conducted with a Cu anode generator operating at 40 kV and 100 mA. (a) Products from HV conditions and various temperatures produced obvious antigorite-related peaks in XRD spectra ($2\theta = \sim 3^\circ\text{--}70^\circ$). (b) Detailed view of part of 10a shows subtle peaks at high temperatures (500°C and 600°C) at $2\theta = 7^\circ\text{--}13^\circ$ and $21^\circ\text{--}36^\circ$, which correspond to talc (001) at $2\theta = 9.5^\circ$, forsterite (120) at $2\theta = 22.9^\circ$, and forsterite (031) at $2\theta = 32.3^\circ$. Talc and forsterite are evidence of antigorite dehydration. XRD spectra for (c) MV and (d) LV conditions show fairly weak forsterite peaks at 450°C.

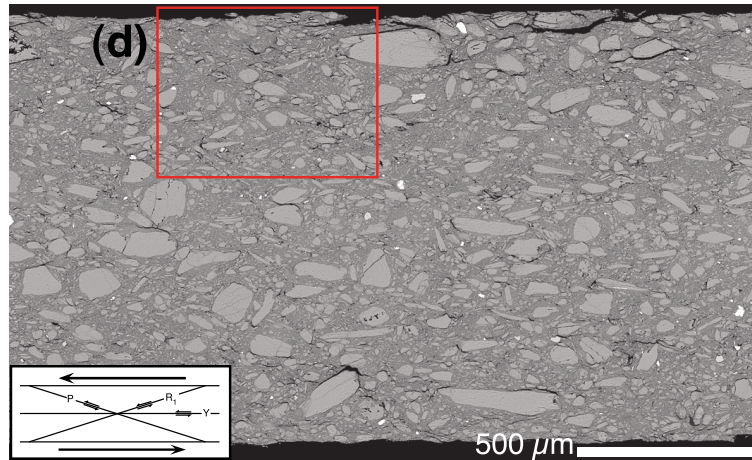
(a) MV 200°C



(b)



(c) LV 200°C



(d)

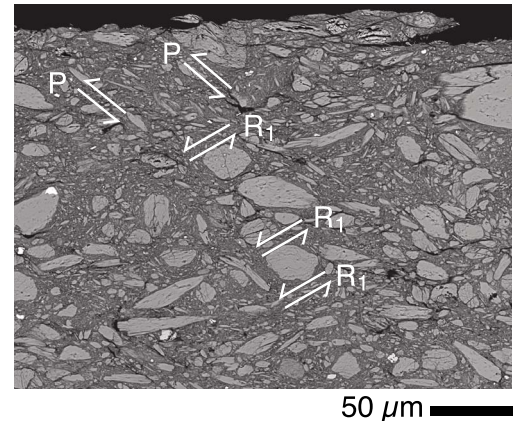


Figure 11. Backscattered-electron SEM images for the experimental products at (T, V) equals (a) (200°C, MV) and (c) (200°C, LV). Enlarged areas in red squares are for (b) (200°C, MV) and (d) (200°C, LV). Both images are from specimens that showed flow behavior in response to stepwise changes in velocity. The Riedel shear structure in 11a is right lateral and in 11c is left lateral. Numerous alignments of comminuted, fine grains surrounding relative larger grains formed in R_1 and P shears (Figures 11b and 11d).

et al. [2004], who found fine olivine grains located within and adjacent to faults at various serpentine unstable pressure conditions (1.7–6 GPa). The dehydration reaction of the antigorite under a deviatoric stress condition would occur in a shear-localized zone preferentially, regardless of whether the Clapeyron slope is positive or negative.

[33] Although there is no clear evidence in the XRD or SEM results of dehydration for $(T, V) = (450^\circ\text{C}, \text{HV})$, gouge behavior responded to stepwise velocity changes by exhibiting the evolution effect in flow behavior. It is possible that forsterite was present in volumes too small to detect in the XRD spectra and at grain sizes too small to recognize under SEM. Talc was invisible in SEM images even though XRD spectra (Figure 10b) of the experimental products at $(T, V) = (600^\circ\text{C}, \text{HV})$ determined the talc. There are two possibilities: (1) talc, having a grain size too fine to be

distinguished, was present in the SEM images, and (2) most of the Si^{4+} involved in the dehydration reaction dissolved in water and escaped from the gouge zone.

6. Discussion

6.1. Shear-Induced Dehydration of Antigorite Gouge

[34] At the dehydration temperature, antigorite gouge exhibited drastic changes in frictional strength and a transient response to stepwise changes in velocity. The (T, V) conditions at which evidence of antigorite dehydration was present (Figure 10 for XRD analyses and Figures 12–13 for SEM images) were also the conditions under which great increases in frictional strength developed (Figure 4) and where the evolution effect was conspicuous (Figures 3 and 6). That increase in frictional strength would not be caused by

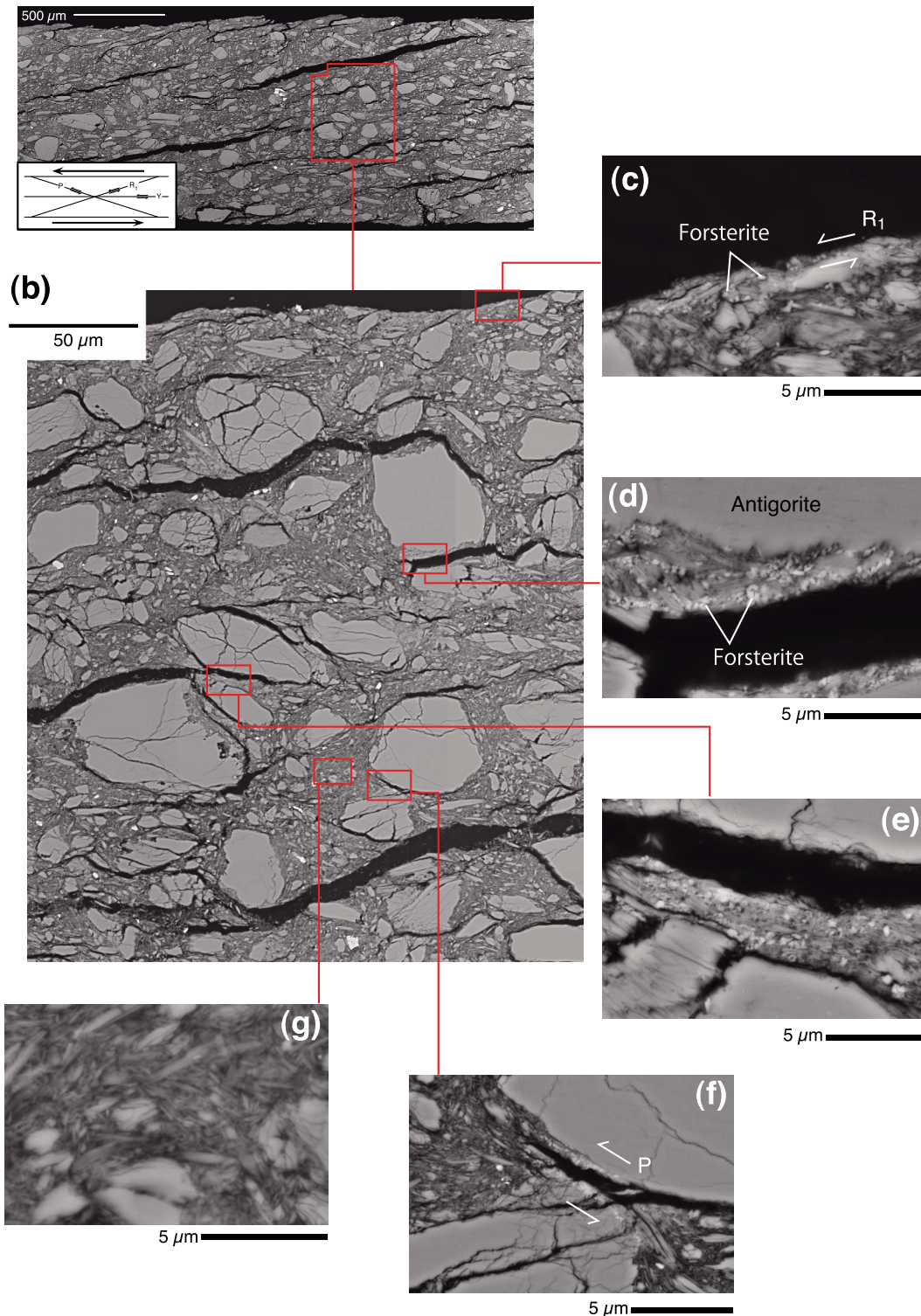
(a) MV 450°C

Figure 12. (a) Backscattered-electron SEM image for an experimental product that exhibited stick-slip behavior (Figure 3b) at $(T, V) = (450^{\circ}\text{C}, \text{MV})$ and that included a small amount of forsterite (Figure 10c). Shearing was sinistral. (b) Magnified view illustrates fine, brighter particles (considered to be forsterite) in shear-localized zones such as (c) Riedel shears and (d–f) comminuted zones among relatively large antigorite grains. Each size of forsterite particle was $<1\ \mu\text{m}$. In the zones of comminuted fine antigorite, the fine forsterite particles had crudely aligned (Figures 10d–10f). (g) Areas of fine-grained antigorite that were not strongly sheared did not contain forsterite grains.

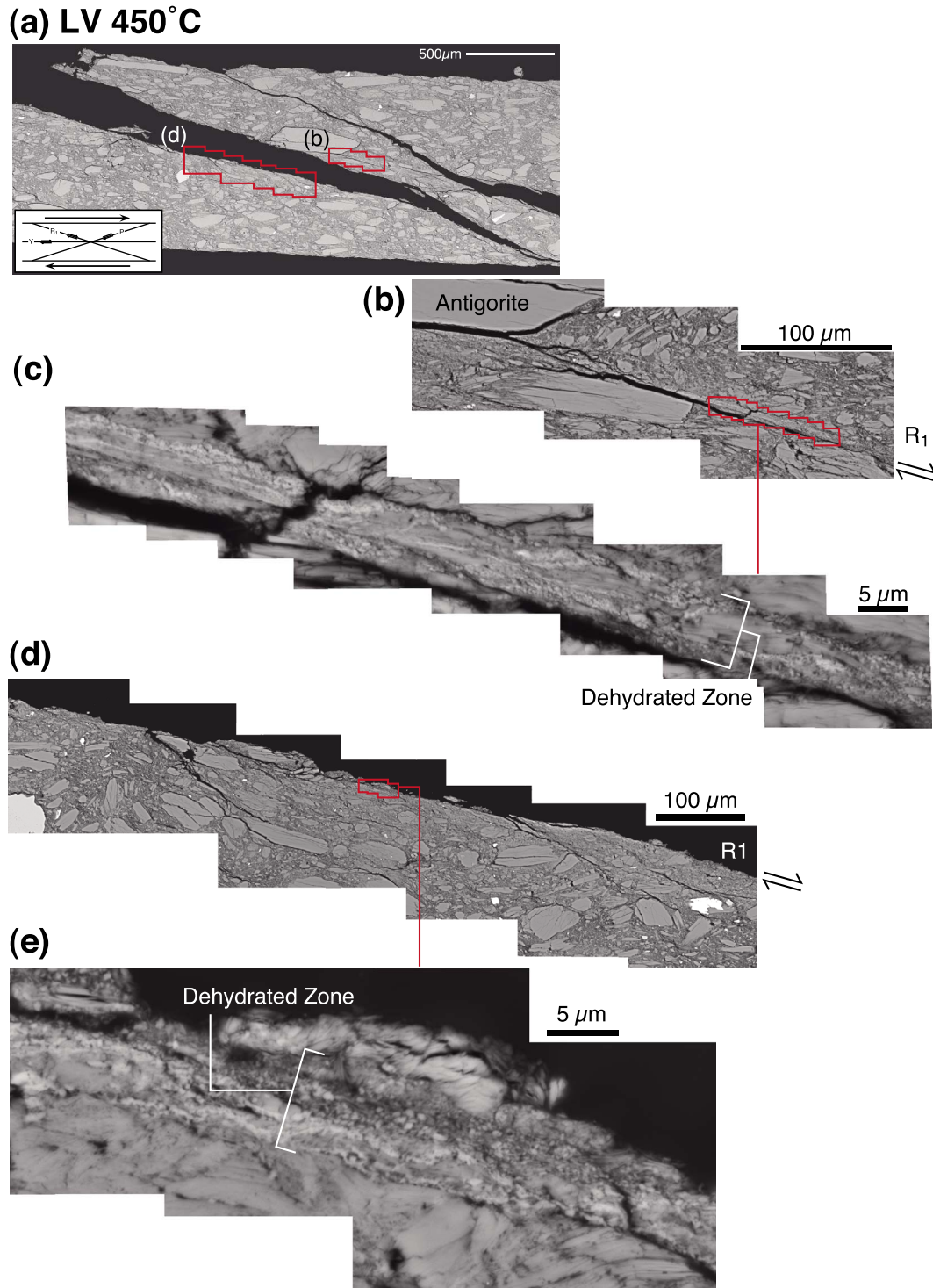


Figure 13. (a) Backscattered-electron SEM images for an experimental product that exhibited stick-slip behavior (Figure 2c) at $(T, V) = (450^\circ\text{C}, \text{LV})$ and contained a small amount of forsterite (Figure 10d). Shearing was dextral. These images demonstrate that dehydration took place only in sheared zones. (b, d) Magnified images showing bright, fine forsterite particles along R_1 shears. (c) Forsterite particles developed along antigorite cleavages in dehydration zones about $5\ \mu\text{m}$ thick. (e) Several narrow zones ($\sim 10\ \mu\text{m}$ thick) containing numerous submicron-sized forsterite particles are concentrated along an R_1 shear.

absorbed, thin-film water from the antigorite (001) surfaces, as noted by *Moore and Lockner* [2004]. If the shear through the water film between the antigorite (001) surfaces had mainly determined the strength of the antigorite gouge, then the friction coefficient would increase gradually from room temperature. Instead, Figure 4 indicates a gradual decrease in strength from room temperature to approximately 200°C.

[35] However, XRD spectra (Figure 10) indicated that the amount of forsterite that formed during the experiment was limited. Submicron-sized forsterite developed preferentially in shear-localized zones, such as Riedel shears, and in zones of comminution between larger antigorite grains (Figures 12 and 13). Antigorite reacted more strongly in shear-localized zones than in lightly sheared areas, even if the original grain size was small (Figure 12g). From these observations, it can be argued that dehydration was shear-induced, and shears containing forsterite were able to dominate both the general strength and the frictional behavior of the gouge.

[36] There are two possible processes of shear-induced dehydration: a mechanochemical reaction or a dilatancy-enhanced reaction. A mechanochemical process would involve mechanical breakage, enhancing the reaction. On the other hand, a dilatancy-induced process would require local temporal dilation and reduction in fluid pressure in shear zones caused by cracking or a grain-boundary opening, which would enhance the dehydration reaction because of the positive Clapeyron slope under both the confining and pore pressure conditions, 100 MPa and 30 MPa, respectively. Additionally, local dilation can harden the apparent strength of the gouge under the undrained condition, i.e., dilatancy hardening.

[37] However, it was previously reported that the solid products (mostly fine olivine) of dehydration preferentially located within and adjacent to faults for P-T conditions at both positive and negative Clapeyron slopes [*Jung et al.*, 2004]. Additionally, fluid diffusivity was measured by the pore pressure oscillation method to be $9.61 \times 10^{-5} \text{ m}^2/\text{s}$ in a sheared antigorite gouge zone, meaning that the pore pressure increase or decrease at $T = 450^\circ\text{C}$ required only 4 s to diffuse from the end of the gouge layer to the center hole of an alumina precut spacer (20 mm distance). (Note that we calculated the diffusivity at $(P_p, T) = (30 \text{ MPa}, 450^\circ\text{C})$ by the measured permeability ($3.64 \times 10^{-19} \text{ m}^2$), the measured storage capacity ($1.23 \times 10^{-4}/\text{MPa}$) of the antigorite gouge, and the water viscosity ($3.09 \times 10^{-11} \text{ MPa/s}$.) Therefore, it would be difficult to maintain locally lower or higher pore pressure in the gouge zone for a long time. The dilation process may not explain the localized dehydration and/or the conspicuous strengthening of the friction at the dehydration temperature, $T \geq 450^\circ\text{C}$.

[38] An additional experiment was carried out to confirm the effect of newly formed forsterite on both the strength and frictional behavior of the gouge (Figure 14). Dehydration was induced at $(T, V) = (500^\circ\text{C}, \text{MV})$, after which the specimen was cooled at $d = 1.1 \text{ mm}$ and at a rate of $\sim 3.3^\circ\text{C}/\text{min}$ toward 400°C to stop dehydration. A higher frictional strength and stick-slip behavior were evident at 500°C . After reduction of the temperature toward 400°C , the friction coefficient decreased during cooling, although it remained higher than that in the case when T was constant at 400°C (orange line in Figure 14a). One important point is that we cannot conclude that the stick-slip behaviors observed at $T \geq 450^\circ\text{C}$ (Figure 3)

did not reflect the alternating increase and decrease in pore pressure that were due to dehydration simply because the stick-slip behavior did not cease immediately after dehydration stopped (Figure 14b). Instead, once a shear fabric affected by dehydration has developed throughout the gouge, it may be difficult for new shear planes to form immediately in the weak antigorite grains. Stick-slip behavior diminished gradually, and positive velocity dependence was apparent with stepwise velocity changes (Figure 14c). A gradual change might occur in the slip plane using the antigorite grains from that affected by the presence of forsterite.

[39] A previous study [*Moore et al.*, 1986] mentioned that evidence of dehydration in serpentine gouge (chrysotile and lizardite) at $(P_c, T) = (100 \text{ MPa}, 400^\circ\text{C})$ developed at lower-velocity conditions because of a lengthy reaction time. A more important point of *Moore et al.*'s findings in 1986 is that serpentine gouge that was heated, without loading, at $T = 400^\circ\text{C}$ for a longer time (66 h) than the length of their deformation experiments did not generate forsterite. It was suggested that increased strain and increased surface energy that were due to deformation promoted the reaction, i.e., a mechanochemical process induced the reaction. The SEM data of the present study, indicating that dehydration occurred only in shear-localized zones, support the implications of *Moore et al.* [1986]. At comparatively low temperatures, dehydration reactions may be triggered by mechanical breakages of the serpentine gouge particles.

[40] From the above discussion, embrittlement at the dehydration temperature could not have been caused by increased pore pressure, known as "dehydration embrittlement" [*Raleigh and Paterson*, 1965]. Water freed by mineral dehydration can be retained temporarily in a low-permeability zone, causing a temporary increase in pore pressure and a reduction in the apparent frictional strength of a fault [*Takahashi et al.*, 2009]. In this study, however, dehydration caused strengthening of the simulated fault (Figure 4). The experimental embrittlement documented in this paper must therefore be a function of the frictional properties of recrystallized minerals, rather than temporary increases in pore pressure. This suggests that faults that contain hydrous minerals such as serpentine can become strengthened and brittle once dehydration begins to take place, regardless of whether the P-T and/or the poroelastic conditions allow the pore pressure to increase.

[41] The question remains of how a gouge consisting predominantly of the structurally weak mineral antigorite could exhibit higher strength after some dehydration. Even after stronger forsterite particles had developed along shear planes, the overall volume of forsterite nucleated during the deformation was volumetrically low relative to the much weaker antigorite (Figure 10). Our observations revealed the presence of streaky forsterite alignments in SEM images (Figures 12 and 13) and suggest how this process might develop. Streaky alignments may develop through repeated shear localization, shear-induced dehydration, and strengthening along a plane, followed by the development of a new shear plane just beside the previous one. After such a process has progressed continuously and at various locations in the shear zones, the overall strength of the gouge might begin to reflect the strength of the forsterite (Figure 4).

[42] We avoided the need to consider the effects of pore pressure changes on the mechanical property of antigorite

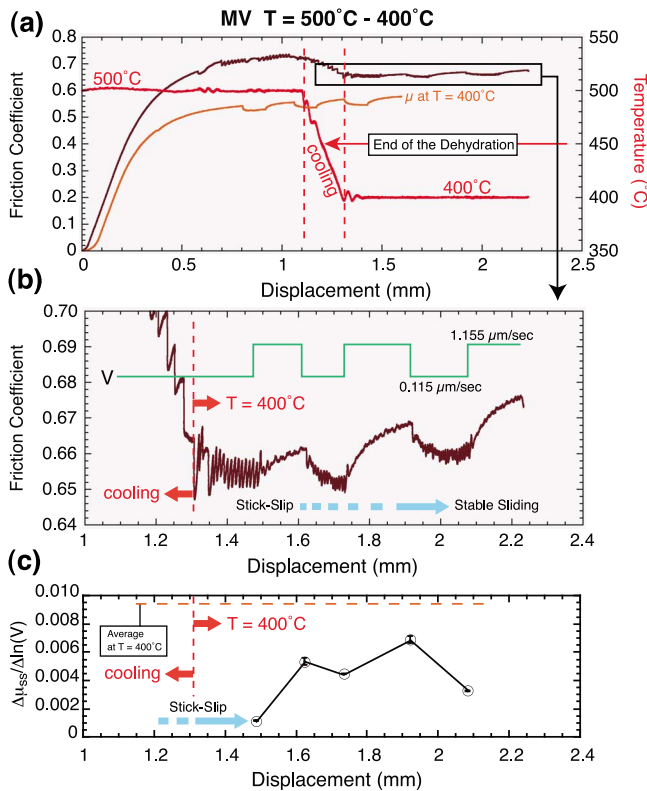


Figure 14. Influence of newly formed forsterite on strength and frictional behaviors during shearing. (a) During shearing, the specimen was cooled at 3.3°C/min at $d = 1.1$ mm from $T = 500^\circ\text{C}$, where dehydration took place, to 400°C , where, under MV conditions, dehydration ceased. After cooling toward 400°C , the friction coefficient (brown line) did not stabilize at the same level as its value at $T = 400^\circ\text{C}$ (orange line), although it did decrease slightly during cooling. (b) Stick-slip behavior at $T = 500^\circ\text{C}$ did not cease immediately after stopping the dehydration but rather diminished gradually, and (c) velocity-dependence became positive with each stepwise change in velocity.

gouge because our experimental conditions were completely “drained.” The mechanical change caused by the shear-induced dehydration would be that of the decomposed solid material, forsterite at $T \geq 450^\circ\text{C}$. We suggest that this shear-induced dehydration in serpentine could be a cause of earthquakes around subduction zones, which have been suggested to be related to serpentine, such as in the lower plane of double seismic zones and nonvolcanic tremors in serpentinized wedge mantle. Regardless of the pore pressure increase or decrease that is due to dehydration, antigorite gouge undergoing localized shear could potentially be involved in seismic slip. We particularly note the possibility that shear-induced dehydration could be a mechanism of nonvolcanic tremors. Shear-induced dehydration can form mechanical heterogeneity in a serpentinized wedge mantle, as found by Ando *et al.* [2010], when imaging seismic patches (locally dehydrated areas) in aseismic flowing serpentine. In several subduction zones, however, nonvolcanic tremors have been observed at different depths, and temperature

models associated with subductions [e.g., Peacock, 2009] showed lower temperatures at the epicenter depth of tremors than at the beginning of antigorite breakdown [Ulmer and Trommsdorff, 1995, for H_2O saturation conditions]. Further studies and discussions of the shear-induced dehydration of antigorite in relation to earthquake mechanisms around subduction zones are needed.

6.2. Rheology of Antigorite

[43] Many previous reports on subsequent changes in friction of rocks and minerals in response to stepwise changes in velocity, such as those depicted in Figures 6c and 6d, have expressed gradual responses as “negative b_2 ” using RSF law (7) [e.g., Weeks and Tullis, 1985; Marone and Cox, 1994; Blanpied *et al.*, 1998; Noda and Shimamoto, 2009]. By measuring changes in the transmissibility of acoustic waves through shear zones, Nagata *et al.* [2008] established that the state variable of equation (7b) was, in fact, directly related to the contact area of the shear surfaces. The behaviors documented included a positive relation between the transmissibility (correlating to the contact area) and the logarithm of contact time, and a negative relation between the transmissibility and $\ln(V)$. Thus, parameter b in equation (7) is related to the ratio of change in the real contact area against $\Delta \ln(V)$ and must be positive if the transient behavior obeys the RSF law. A negative b_2 in the RSF law was not assumed in the present study; instead a system including a series of spring dampers with parameters k_2 and a_2 was employed. (Computationally, a_2 and k_2 are equivalent to $-b_2$ and $-b_2/Dc_2$, respectively, if negative b_2 must be accommodated.)

[44] Reinen *et al.* [1994] suggested that a possible process for flow in serpentine (antigorite and lizardite) was a “dislocation glide,” a phenomenon that had been observed in the deformation of biotite [Kronenberg *et al.*, 1990]. Dislocation gliding along the basal cleavage of a sheet silicate would be easier than in other silicate minerals because of the low bond strengths along the (001) plane. Recently, Noda and Shimamoto [2010], observing the flow behavior in polycrystalline halite at high temperatures, suggested that the gradual changes in shear stress following a stepwise change in velocity could result from a competition between work hardening and recovery from work hardening. In the present study, the flow mechanism characterized by the parameter a_2 may function within antigorite grains, as in the previous examples. The transient response of antigorite flow would correspond to a modification of an intergranular structure in response to changes in velocity, work hardening, and relaxation. Parameter a_2 increased with increasing T and decreasing velocity, and the temperature at which a_2 became effective was lower at lower velocities (Figure 8). This feature of a_2 suggests a (relatively simple) thermally activated process, although the specific mechanism cannot be identified at this time. Characterizing the mechanism of intragranular deformation will require additional experiments at lower-velocity conditions than those used in this study.

[45] In contrast to parameter a_2 , the dependence of frictional parameter a_1 on (T, V) conditions is quite complicated (Figure 9). Nakatani [2001] expressed the relationship theoretically as

$$a_1 = kT/vp, \quad (10)$$

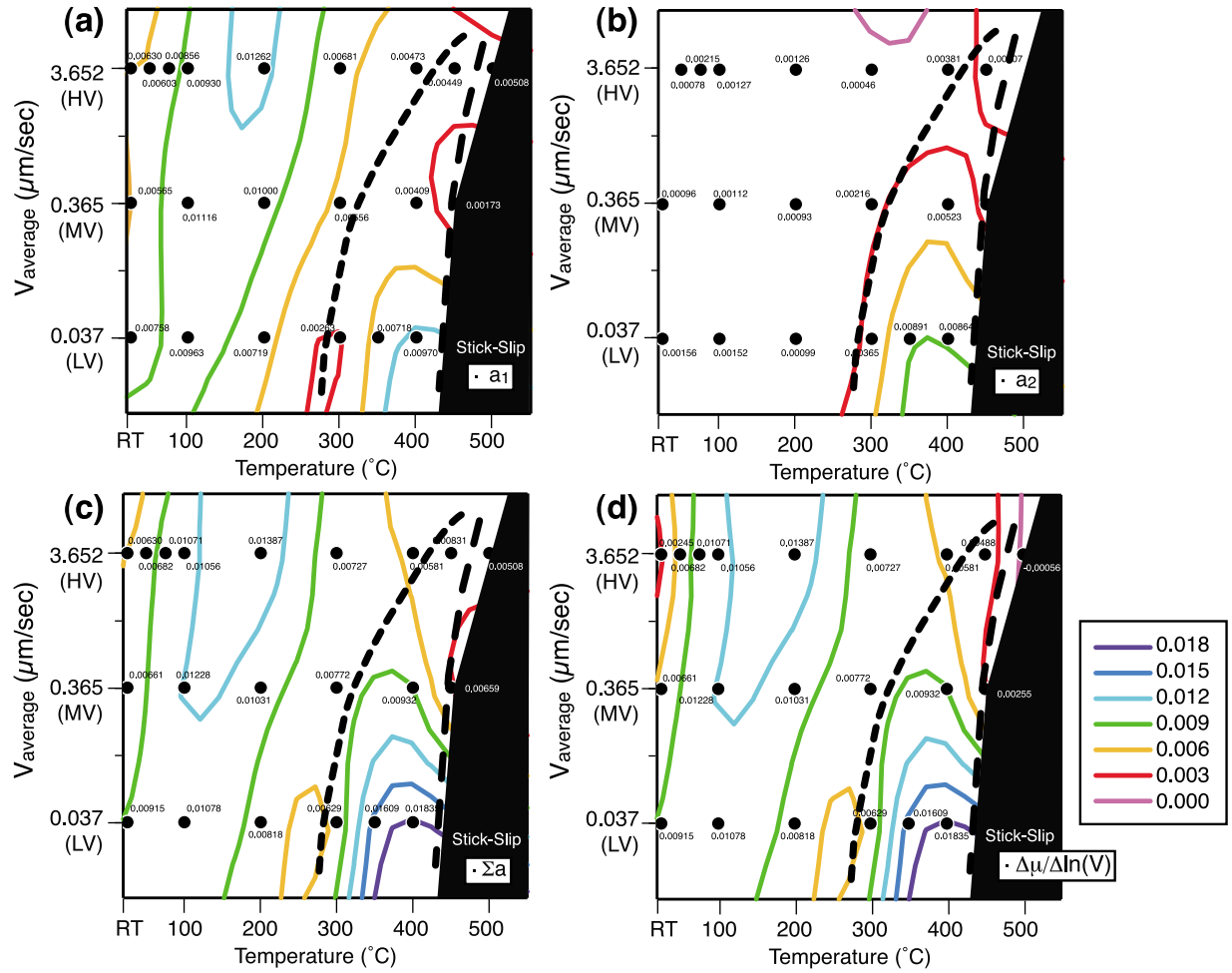


Figure 15. Contour maps of the average parameters of (a) a_1 , (b) a_2 , (c) Σa , and (d) $\Delta\mu_{ss}/\Delta \ln V$ (Table 2) for a range of (T, V) conditions. The field dominated by stick-slip behavior is black. A long-dashed line indicates a possible mechanical boundary between flow behavior and frictional behavior. A short-dashed line denotes another mechanical boundary where the intragranular flow behavior begins to appear.

where k is the Boltzmann constant (in joules per Kelvin), v is an activation volume (in cubic meters), and p is an index of hardness (in pascals). Nakatani [2001] showed that in albite gouges, a_1 increased linearly with increasing temperature because both v and p of the albite would be nearly constant for those temperature conditions (25°C–800°C). Perhaps antigorite gouge also has interdependences among p , v , and T .

[46] Preliminary contour maps (Figure 15) show parameters a_1 , a_2 , Σa , and $\Delta\mu_{ss}/\Delta \ln V$ (summarized in Table 2) for given (T, V) conditions. Such maps could help to elucidate complicated interdependences among parameters and deformation conditions. Contours could not be constructed for stick-slip behavior because the parameters could not be determined; these parts of the maps are thus blacked out. When the frictional behavior (including stick-slip) appeared above $T = 450^\circ\text{C}$ – 500°C because of antigorite dehydration, it differed markedly from the predominant flow behavior. The mechanical boundary between flow behavior and frictional behavior is indicated by a long dashed line. The contour map for a_1 (Figure 15a) provides understandable information about the relationship between a_1 and (T, V) . A zone of minimum a_1 is sandwiched by two larger a_1 areas.

In general, the contour lines for a_1 are roughly parallel, with a strong dependence on T and a slight dependence on $\log(V)$. A mechanical boundary in the a_2 map (Figure 15) is indicated with a short dashed line, indicating where intragranular flow behavior became evident (Figure 8). Contour lines and mechanical boundaries have generally similar orientations in (T, V) space, and the mechanical boundaries for dehydration and for visible flow both depended more strongly on temperature than on velocity. The distribution of $\Delta\mu_{ss}/\Delta \ln V$ in this (T, V) regime (Figure 15d) differs slightly from that of Σa (Figure 15c) because the reduction in Σb appeared at both room temperature and at $\geq 450^\circ\text{C}$ under the HV conditions.

[47] Contour maps of experimental parameters may also be useful for simulating the movement of serpentine-bearing faults, although the complicated nature of the deformation precluded identification of the movement mechanisms in this study. Contour maps will permit the identification of favorable conditions for strain localization and allow the evaluation of the earthquake potential of serpentine-bearing faults, such as the San Andreas fault or subducting plates in contact with a serpentinized mantle wedge (like that in southwest

Japan). These maps should be expanded to include new data for different velocity conditions (both higher and lower).

7. Conclusions

[48] The frictional properties of serpentinite are of particular interest in the study of earthquake-generating processes along subducting plates and transform faults. To understand the rheology of serpentine-bearing faults comprehensively, the transient response of serpentinite to stepwise changes in slip velocity under high-temperature conditions was investigated. Shear-sliding tests were undertaken using a gas-medium, high-pressure, and high-temperature triaxial testing machine to investigate the rheology of serpentinite (antigorite) gouge. Sliding deformation was applied to a thin layer of gouge (~0.8 mm) sandwiched between two alumina blocks under various temperature conditions (from room temperature to 600°C). All experiments were carried out under a constant confining pressure (100 MPa) and a constant pore water pressure (30 MPa). Because the pore pressure was held constant, the fluid flow condition was of a “drained” type. At each temperature, the transient response of frictional characteristics following stepwise changes in the slip velocity was documented; slip velocity varied between 0.0115 μm/s ($\sim 1.4 \times 10^{-5}$) and 11.5 mm/s ($\sim 1.4 \times 10^{-2}$).

[49] Both the general level of frictional strength and the transient responses to stepwise changes in velocity changed drastically at around 450°C. As the temperature was increased from 400°C to 450°C, the strength of antigorite at 1.2 mm displacement rose sharply, by as much as ~ 0.15 in terms of the friction coefficient (Figure 4). The transient response also indicated a change in the mode of deformation from a flow-type behavior at temperatures below 400°C to a frictional behavior (stick-slip) at temperatures above 450°C–500°C (e.g., Figure 6). XRD spectra of the experimental products at higher temperatures exhibited several peaks that correspond to forsterite, implying that dehydration had taken place (Figure 10). However, the intensities of these peaks in the XRD spectra were fairly weak, indicating that only a limited volume of the serpentinite had been involved in the reaction. SEM imaging demonstrated that submicron-sized forsterite particles, commonly forming streaky alignments, were present only along shear-localized zones (microscopic Riedel shears) and/or zones of comminution among relatively larger antigorite grains (Figures 12 and 13). Serpentine in microscopic shear-localized zones reacted preferentially, suggesting shear-induced dehydration. Owing to the drained condition, embrittlement at the dehydration-inducing temperature could not have been caused by an increase in pore pressure. This suggests that faults containing hydrous minerals such as serpentinite can become strengthened and brittle once dehydration begins to take place, even if the P-T and/or the poroelastic conditions do not allow the pore pressure to increase. The harder mineral, forsterite, even in fairly small amounts, will control both the strength and the behavior of the serpentinite-dominated gouge as long as dehydration proceeds.

[50] Transient responses to stepwise changes in slip velocity reflect the rheology of the antigorite gouge. Flow-type behavior, showing no evolution effects in the transient response, dominated under the deformation conditions of these experiments. The flow behavior was modeled by com-

binning a direct effect (with parameter a_1 for instantaneous response) with a spring-damper model (with parameters a_2 and k_2 for subsequent increase in friction per $\Delta \ln V$). Changes in friction after changes in velocity resembled those of a viscous damper and were associated with a modification of the intergranular structure.

[51] Contour maps of the average parameters a_1 , a_2 , Σa , and $\Delta \mu_{ss}/\Delta \ln V$ (Figure 15), summarize the relationships among parameters and temperature and velocity conditions, showing complicated dependences on both temperature and velocity. Parameter a_2 , however, showed a fairly simple increase in response to increased temperature and decreased velocity; the temperature at which a_2 became effective was lower at lower velocity (Figure 15b). These features of a_2 suggest a relatively simple, thermally activated process. Although the exact mechanism of flow in antigorite gouge could not be identified, contour maps for the parameters can identify conditions that are favorable for strain localization and facilitate evaluation of earthquake potential for serpentine-bearing faults such as the San Andreas fault or any subducting plate that is in contact with a serpentinized mantle wedge (e.g., as found in southwest Japan). Future work on extending the maps should focus on including a wider range of experimental conditions.

Appendix A: Responses in Complex Models to Positive and Negative Stepwise Velocity Changes

[52] According to *Noda and Shimamoto* [2009], transient responses to stepwise changes in slip velocity depended on whether the velocity change was positive or negative. Moreover, the transient responses varied according to where the displacement was measured in the experimental device. The explanation for why the apparent distance (d_{ss}) for next steady state friction (μ_{ss}) should be different for positive and negative velocity steps was arrived at using a set of constitutive parameters: instantaneous response a_1 and normalized machine stiffness k_1 . According to *Noda and Shimamoto* [2009], the change in friction coefficient $\Delta \mu$ could be expressed by

$$\Delta \dot{\mu} = a_1 \cdot \frac{\dot{V}_{body}}{V_{body}} \quad (\text{A1a})$$

$$\Delta \dot{\mu} = k_1 (V_{lp} - V_{body}). \quad (\text{A1b})$$

The solution V_{body} was obtained from equations (A1), giving

$$V_{body} = \frac{V_{lp}}{2} \left(1 + \tanh \left(t \cdot \frac{k_1 V_{lp}}{2a_1} \right) - 1.009 \right) \quad (\text{A2a})$$

(10 times gain in V_{lp}) and

$$V_{body} = \frac{V_{lp}}{2} \left(1 + \coth \left(t \cdot \frac{k_1 V_{lp}}{2a_1} \right) + 5.368 \times 10^{-2} \right) \quad (\text{A2b})$$

(10 times loss in V_{lp}).

[53] To let μ become μ_{ss} , a critical time had to elapse after the change in velocity: $t_c = 4a_1/k_1 V_{lp}$ for a 10-fold increase in velocity, and $t_c = 2a_1/k_1 V_{lp}$ for a 10-fold decrease in

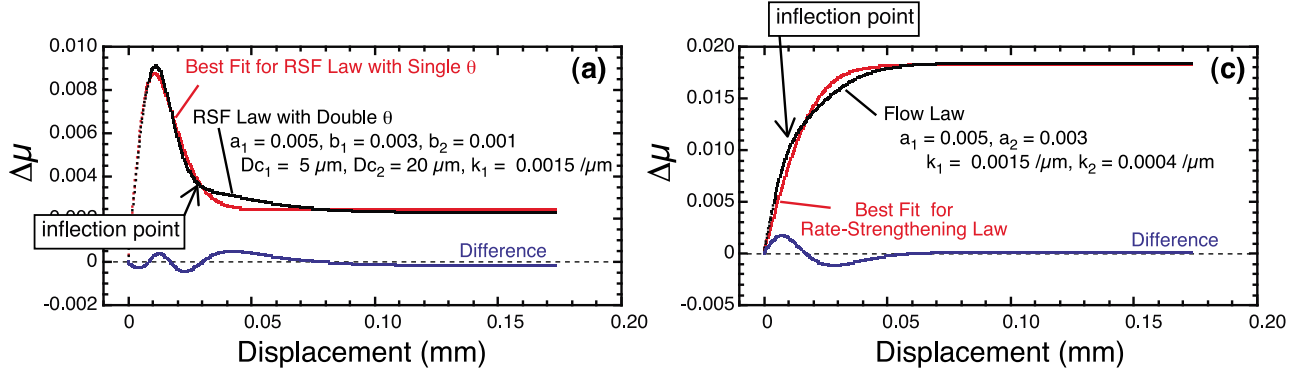
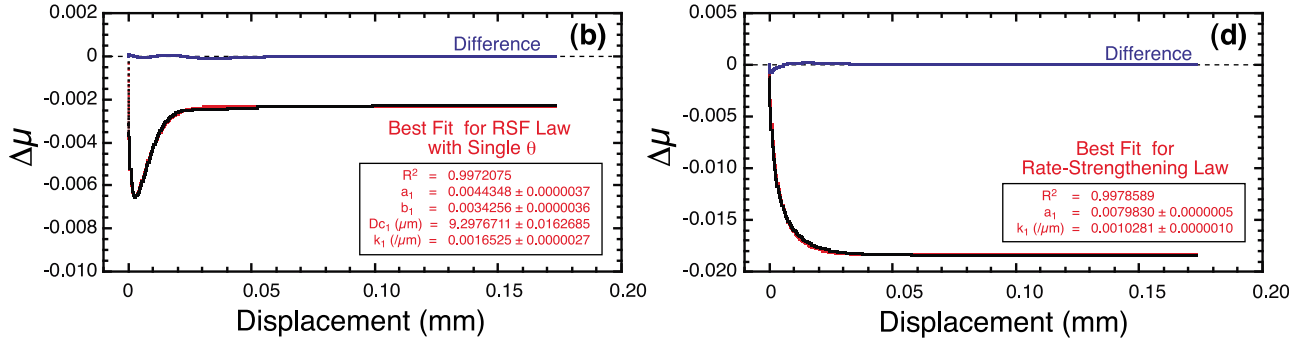
Positive Velocity Step ($V = 10V_0$)Negative Velocity Step ($V = 0.1V_0$)

Figure A1. Simulated data for (a) a stepwise velocity increase and (b) a stepwise velocity decrease by a factor of 10 for the RSF constitutive law with two state variables (black dots) and the RSF constitutive law with one state variable (red dots). Same data for (c) stepwise velocity increase and (d) stepwise velocity decrease by a factor of 10 for flow law (black dots), and their fitting result using a simple model accompanied by only a direct effect (red dots). For stepwise velocity increases (Figures A1a and A1c), differences (blue dots) between black dots and red dots were conspicuous near the points of inflection shown in the complex models. However, the differences for stepwise velocity decreases (Figures A1b and A1d) were indistinguishable, producing a high correlation coefficient (>0.99) with fitting results that used simpler models.

velocity (see Figure 7 of *Noda and Shimamoto* [2009]). The distance d_{ss} for μ_{ss} could then be written as

$$d_{ss} = \int_0^{t_c} V dt. \quad (\text{A3})$$

In cases in which it is possible to measure displacement near the specimen, for example, in a biaxial shearing system [*Noda and Shimamoto*, 2009], $V = V_{\text{body}}$ in equation (A3). In the present study, displacement was measured at the loading point, $V = V_{\text{lp}}$ in equation (A3). Therefore, d_{ss} measured at the loading point will be $4a_1/k_1$ for a 10-fold increase in velocity and $2a_1/k_1$ for a 10-fold decrease in velocity. Experimental results showed that the apparent distances that allow μ to be in a steady state after a positive velocity change were approximately twice as large as those for a negative velocity change (Figure 5b).

[54] The models used were complicated owing to the inclusion of numerous parameters: $(a_1, b_1, b_2, Dc_1, Dc_2, k_1)$ in the RSF constitutive law with two state variables (equation (7)) and (a_1, a_2, k_1, k_2) in the flow law (equation (8)). It is necessary to address differences in the change in friction between

positive velocity changes and negative velocity changes for the RSF law with two state variables and for the flow law.

[55] Figure A1a shows the simulated data for a velocity increase by a factor of 10 for the RSF constitutive law with two state variables (black dots), where the parameters $(a_1, b_1, b_2, Dc_1, Dc_2, k_1) = (0.005, 0.003, 0.001, 5 \mu\text{m}, 20 \mu\text{m}, 0.0015/\mu\text{m})$, respectively, which are the expected values in this study. Using a simpler model with the RSF law with one state variable, a best fit curve and optimized parameters (a_1, b_1, Dc_1, k_1) can be obtained. However, the best fit curve does not match the combined data, which implies that the model chosen should be easily determined based on the shape of the friction curve. Likewise, in the case of the flow law (Figure A1c), the grouped data for positive velocity steps for the flow law, $(a_1, a_2, k_1, k_2) = (0.005, 0.003, 0.0015/\mu\text{m}, 0.0004/\mu\text{m})$, do not agree with the best fit curve using the simpler model, which requires parameters a_1 and k_1 only. Both the RSF law with two state variables and the flow law at positive velocity changes exhibit obvious inflection points in the transient responses (Figures A1a and A1c). Transient responses to the negative velocity changes (Figures A1b and A1d) were smoother than those for positive velocity changes, even when the parameters had the same

values. In both models, the inflection points were indistinct. The fitting curves using simpler models correlated well with the grouped data, with $R^2 > 0.99$. In real measurements, there was no meaningful difference between the complex model and the simple model for negative velocity changes because of noise. For this reason it is difficult to obtain optimized parameters for negative velocity changes using a complex model, such as equations (7)–(9).

[56] **Acknowledgments.** We thank three reviewers, an anonymous reviewer, Chris Spiers, and Diane Moore for their kindly encouragements and fruitful comments. Discussions of frictional behaviors with Masao Nakatani and Toshi Shimamoto provided helpful guidance in understanding serpentine behavior. Hiroyuki Noda helped to code a program for the iterative least squares curve fitting. Ikuo Cho calculated the optimized contour lines. We also thank Ikuo Katayama for helping us to measure the fluid flow properties of the antigorite gouge at Hiroshima University when our testing machine was damaged by the 2011 earthquake off the Pacific coast of Tohoku. This work was partly supported by a Science Research grant (22340148: Ichiko Shimizu) from the Japan Society for the Promotion of Science, and also supported by the Ministry of Education, Culture, Sports, Science and Technology (MEXT) of Japan, under its Observation and Research Program for Prediction of Earthquakes and Volcanic Eruptions.

References

- Ando, R., R. Nakata, and T. Hori (2010), A slip pulse model with fault heterogeneity for low-frequency earthquakes and tremor along plate interface, *Geophys. Res. Lett.*, **37**, L10310, doi:10.1029/2010GL043056.
- Blanpied, M. L., C. J. Marone, D. A. Lockner, J. D. Byerlee, and D. P. King (1998), Quantitative measure of the variation in fault rheology due to fluid-rock interactions, *J. Geophys. Res.*, **103**, 9691–9712, doi:10.1029/98JB00162.
- Brune, J. N., T. L. Henyey, and R. F. Roy (1969), Heat flow, stress and rate of slip along the San Andreas fault, California, *J. Geophys. Res.*, **74**, 3821–3827, doi:10.1029/JB074i015p03821.
- Chernak, L. J., and G. Hirth (2010), Deformation of antigorite serpentine at high temperature and pressure, *Earth Planet. Sci. Lett.*, **296**, 23–33, doi:10.1016/j.epsl.2010.04.035.
- Christensen, N. (1972), The Abundance of Serpentinities in the Oceanic Crust, *J. Geol.*, **80**, 709–719, doi:10.1086/627796.
- Collettini, C., A. Niemeijer, C. Viti, and C. Marone (2009), Fault zone fabric and fault weakness, *Nature*, **462**, 907–910, doi:10.1038/nature08585.
- Dieterich, J. H. (1979), Modeling of rock friction: 1. Experimental results and constitutive equations, *J. Geophys. Res.*, **84**, 2161–2168, doi:10.1029/JB084iB05p02161.
- Dieterich, J. H. (1981), Constitutive properties of faults with simulated gouge, in *Mechanical Behavior of Crustal Rocks*, *Geophys. Monogr. Ser.*, vol. 24, edited by N. L. Carter, J. M. Logan, and D. W. Stearns, pp. 103–120, AGU, Washington, D. C.
- Dieterich, J. H., and B. D. Kilgore (1994), Direct observation of frictional contacts; new insights for state-dependent properties, *Pure Appl. Geophys.*, **143**, 283–302, doi:10.1007/BF00874332.
- Evans, B. W., W. Johannes, H. Oterdoom, and V. Trommsdorff (1976), Stability of chrysotile and antigorite in the serpentine multisystems, *Schweiz. Mineral. Petrogr. Mitt.*, **56**, 79–93.
- Fischer, G. J., and M. S. Paterson (1992), Measurement of permeability and storage capacity in rocks during deformation at high temperature and pressure, in *Fault Mechanics and Transport Properties of Rocks*, edited by B. Evans and T.-F. Wang, pp. 213–252, Elsevier, New York, doi:10.1016/S0074-6142(08)62824-7.
- Hacker, B. R., S. M. Peacock, G. A. Abers, and S. D. Holloway (2003a), Subduction factory 1. Theoretical mineralogy, densities, seismic wave speeds, and H₂O contents, *J. Geophys. Res.*, **108**(B1), 2030, doi:10.1029/2001JB001129.
- Hacker, B. R., S. M. Peacock, G. A. Abers, and S. D. Holloway (2003b), Subduction factory: 2. Are intermediate-depth earthquakes in subducting slabs linked to metamorphic dehydration reactions?, *J. Geophys. Res.*, **108**(B1), 2030, doi:10.1029/2001JB001129.
- Hatano, T. (2011), Power-law rheology and the dynamical heterogeneity in a sheared granular material, *J. Phys. Conf. Ser.*, in press.
- Hilaret, N., and B. Reynard (2009), Stability and dynamics of serpentine layer in subduction zone, *Tectonophysics*, **465**, 24–29, doi:10.1016/j.tecto.2008.10.005.
- Hilaret, N., B. Reynard, Y. Wang, I. Daniel, S. Merkel, N. Nishiyama, and S. Petitgirard (2007), High-pressure creep of serpentine, interseismic deformation, and initiation of subduction, *Science*, **318**, 1910–1913, doi:10.1126/Science.1148494.
- Ide, S., G. C. Beroza, D. R. Shelly, and T. Uchide (2007), A scaling law for slow earthquakes, *Nature*, **447**, 76–79, doi:10.1038/nature05780.
- Iwamori, H. (1998), Transportation of H₂O and melting in subduction zones, *Earth Planet. Sci. Lett.*, **160**, 65–80, doi:10.1016/S0012-821X(98)00080-6.
- Jung, H., H. W. Green II, and L. F. Dobrzinetskaya (2004), Intermediate-depth earthquake faulting by dehydration embrittlement with negative volume change, *Nature*, **428**, 545–549, doi:10.1038/nature02412.
- Jung, H., Y. Fei, P. G. Silver, and H. W. Green II (2009), Frictional sliding in serpentine at very high pressure, *Earth Planet. Sci. Lett.*, **277**, 273–279, doi:10.1016/j.epsl.2008.10.019.
- Kamiya, S., and Y. Kobayashi (2000), Seismological evidence for the existence of serpentinized wedge mantle, *Geophys. Res. Lett.*, **27**, 819–822, doi:10.1029/1999GL011080.
- Kawamoto, E., and T. Shimamoto (1998), The strength profile for bimineralic shear zones; an insight from high-temperature shearing experiments on calcite-halite mixtures, *Tectonophysics*, **295**, 1–14, doi:10.1016/S0040-1951(98)00112-7.
- Kronenberg, A., S. Kirby, and J. Pinkston (1990), Basal slip and mechanical anisotropy of biotite, *J. Geophys. Res.*, **95**(B12), 19,257–19,278, doi:10.1029/JB095iB12p19257.
- Logan, J. M., and K. A. Rauenzahn (1987), Frictional dependence of gouge mixed of quartz montmorillonite on velocity, composition and fabric, *Tectonophysics*, **144**, 87–108, doi:10.1016/0040-1951(87)90010-2.
- Marone, C. (1998), Laboratory-derived friction laws and their application to seismic faulting, *Annu. Rev. Earth Planet. Sci.*, **26**, 643–696, doi:10.1146/annurev.earth.26.1.643.
- Marone, C., and S. J. Cox (1994), Scaling of rock friction constitutive parameters: The effect of surface roughness and cumulative offset on friction of gabbro, *Pure Appl. Geophys.*, **143**, 359–385, doi:10.1007/BF00874335.
- Masuda, K., K. Fujimoto, and T. Arai (2002), A new gas-medium, high-pressure and high-temperature deformation apparatus at AIST, Japan, *Earth Planets Space*, **54**, 1091–1094.
- Matsubara, M., K. Obara, and K. Kasahara (2009), High- V_p/V_s zone accompanying non-volcanic tremors and slow-slip events beneath southwestern Japan, *Tectonophysics*, **472**, 6–17, doi:10.1016/j.tecto.2008.06.013.
- Moore, D. E., and D. A. Lockner (2004), Crystallographic controls on the frictional behavior of dry and water-saturated sheet structure minerals, *J. Geophys. Res.*, **109**, B03401, doi:10.1029/2003JB002582.
- Moore, D. E., and D. A. Lockner (2008), Talc friction in the temperature range 25°–400°C: Relevance for fault-zone weakening, *Tectonophysics*, **449**, 120–132, doi:10.1016/j.tecto.2007.11.039.
- Moore, D. E., and D. A. Lockner (2011), Frictional strength of talc-serpentine and talc-quartz mixtures, *J. Geophys. Res.*, **116**, B01403, doi:10.1029/2010JB007881.
- Moore, D. E., and M. J. Rymer (2007), Talc-bearing serpentine and the creeping section of the San Andreas fault, *Nature*, **448**, 795–797, doi:10.1038/nature06064.
- Moore, D. E., R. Summers, and J. D. Byerlee (1986), The effects of sliding velocity on the frictional and physical properties of heated fault gouge, *Pure Appl. Geophys.*, **124**, 31–52, doi:10.1007/BF00875718.
- Moore, D. E., D. A. Lockner, R. Summer, M. Shengli, and J. D. Byerlee (1996), Strength of chrysotile-serpentine gouge under hydrothermal conditions: Can it explain a weak San Andreas fault?, *Geology*, **24**, 1041–1044, doi:10.1130/0091-7613(1996)024<1041:SOCSSG>2.3.CO;2.
- Moore, D., D. Lockner, M. Shengli, R. Summers, and J. Byerlee (1997), Strengths of serpentine gouges at elevated temperatures, *J. Geophys. Res.*, **102**(B7), 14,787–14,801, doi:10.1029/97JB00995.
- Morrow, C. A., D. E. Moore, and D. A. Lockner (2000), The effect of mineral bond strength and adsorbed water on fault gouge frictional strength, *Geophys. Res. Lett.*, **27**(6), 815–818, doi:10.1029/1999GL008401.
- Nagata, K., M. Nakatani, and S. Yoshida (2008), Monitoring frictional strength with acoustic wave transmission, *Geophys. Res. Lett.*, **35**, L06310, doi:10.1029/2007GL033146.
- Nakatani, M. (2001), Conceptual and physical clarification of rate and state friction: Frictional sliding as a thermally activated rheology, *J. Geophys. Res.*, **106**(B7), 13,347–13,380, doi:10.1029/2000JB000453.
- Noda, H., and T. Shimamoto (2009), Constitutive properties of clayey fault gouge from the Hanaore fault zone, southwest Japan, *J. Geophys. Res.*, **114**, B04409, doi:10.1029/2008JB005683.
- Noda, H., and T. Shimamoto (2010), A rate- and state-dependent ductile flow law of polycrystalline halite under large shear strain and implications for transition to brittle deformation, *Geophys. Res. Lett.*, **37**, L09310, doi:10.1029/2010GL042512.

- Obara, K. (2002), Nonvolcanic deep tremor associated with subduction in southwest Japan, *Science*, 296, 1679–1681, doi:10.1126/science.1070378.
- Peacock, S. M. (2001), Are the lower planes of double seismic zones caused by serpentine dehydration in subducting oceanic mantle?, *Geology*, 29, 299–302, doi:10.1130/0091-7613(2001)029<0299:ATLPOD>2.0.CO;2.
- Peacock, S. M. (2009), Thermal and metamorphic environment of subduction zone episodic tremor and slip, *J. Geophys. Res.*, 114, B00A07, doi:10.1029/2008JB005978.
- Raleigh, C. B., and M. S. Paterson (1965), Experimental deformation of serpentinite and its tectonic implications, *J. Geophys. Res.*, 70, 3965–3985, doi:10.1029/JZ070i016p03965.
- Reinen, L., and J. Weeks (1993), Determination of rock friction constitutive parameters using an iterative least squares inversion method, *J. Geophys. Res.*, 98(B9), 15,937–15,950, doi:10.1029/93JB00780.
- Reinen, L. A., J. D. Weeks, and T. E. Tullis (1991), The frictional behavior of serpentinite: Indications for aseismic creep on shallow crustal faults, *Geophys. Res. Lett.*, 18(10), 1921–1924, doi:10.1029/91GL02367.
- Reinen, L. A., T. E. Tullis, and J. D. Weeks (1992), Two-mechanism model for frictional sliding of serpentinite, *Geophys. Res. Lett.*, 19(15), 1535–1538, doi:10.1029/92GL01388.
- Reinen, L. A., J. D. Weeks, and T. E. Tullis (1994), The frictional behavior of lizardite and antigorite serpentinites: Experiments, constitutive models implications for natural faults, *Pure Appl. Geophys.*, 143(1–3), 317–358, doi:10.1007/BF00874334.
- Seno, T., D. Zhao, Y. Kobayashi, and M. Nakamura (2001), Dehydration of serpentinized slab mantle: Seismic evidence from southwest Japan, *Earth Planets Space*, 53, 861–871.
- Shimamoto, T. (1985), The origin of large or great thrust-type earthquakes along subducting plate boundaries, *Tectonophysics*, 119, 37–65, doi:10.1016/0040-1951(85)90032-0.
- Takahashi, M., K. Mizoguchi, K. Kitamura, and K. Masuda (2007), Effects of clay content on the frictional strength and fluid transport property of faults, *J. Geophys. Res.*, 112, B08206, doi:10.1029/2006JB004678.
- Takahashi, M., K. Mizoguchi, and K. Masuda (2009), Potential of phyllosilicate dehydration and dehydroxylation reactions to trigger earthquakes, *J. Geophys. Res.*, 114, B02207, doi:10.1029/2008JB005630.
- Ulmer, P., and V. Trommsdorff (1995), Serpentine stability to mantle depths and subduction-related magmatism, *Science*, 268, 858–861, doi:10.1126/science.268.5212.858.
- Weeks, J., and T. Tullis (1985), Frictional sliding of dolomite: A variation in constitutive behavior, *J. Geophys. Res.*, 90(B9), 7821–7826, doi:10.1029/JB090iB09p07821.
- Zoback, M. D., et al. (1987), New evidence for the state of stress on the San Andreas fault system, *Science*, 238, 1105–1111, doi:10.1126/science.238.4830.1105.
- K. Masuda and M. Takahashi (corresponding author), Geological Survey of Japan, AIST, Central-7, 1-1-1 Higashi, Tsukuba, Ibaraki 305-8567, Japan. (miki.takahashi@aist.go.jp)
- K. Mizoguchi, Civil Engineering Research Laboratory, Central Research Institute of Electric Power Industry, Abiko 270-1194, Japan.
- K. Okazaki, Department of Earth and Planetary Systems Science, Graduate School of Science, Hiroshima University, Higashi-Hiroshima 736-8526, Japan.
- I. Shimizu, Department of Earth and Planetary Science, Graduate School of Science, University of Tokyo, Tokyo 113-0033, Japan.
- S.-I. Uehara, Department of Environmental Science, Faculty of Science, Toho University, Funabashi 274-8510, Japan.